



Limits of the seismogenic zone in the epicentral region of the 26 December 2004 great Sumatra-Andaman earthquake: Results from seismic refraction and wide-angle reflection surveys and thermal modeling

F. Klingelhoefer,¹ M.-A. Gutscher,² S. Ladage,³ J.-X. Dessa,⁴ D. Graindorge,² D. Franke,³ C. André,² H. Permana,⁵ T. Yudistira,⁶ and A. Chauhan⁷

Received 27 April 2009; revised 23 August 2009; accepted 15 September 2009; published 27 January 2010.

[1] The 26 December 2004 Sumatra earthquake ($M_w = 9.1$) initiated around 30 km depth and ruptured 1300 km of the Indo-Australian–Sunda plate boundary. During the Sumatra-OBS (ocean bottom seismometer) survey, a wide-angle seismic profile was acquired across the epicentral region. A seismic velocity model was obtained from combined travel time tomography and forward modeling. Together with reflection seismic data from the SeaCause II cruise, the deep structure of the source region of the great earthquake is revealed. Four to five kilometers of sediments overlie the oceanic crust at the trench, and the subducting slab can be imaged down to a depth of 35 km. We find a crystalline backstop 120 km from the trench axis, below the fore-arc basin. A high-velocity zone at the lower landward limit of the ray-covered domain, at 22 km depth, marks a shallow continental Moho, 170 km from the trench. The deep structure obtained from the seismic data was used to construct a thermal model of the fore arc in order to predict the limits of the seismogenic zone along the plate boundary fault. Assuming 100° – 150° C as its updip limit, the seismogenic zone is predicted to begin 5–30 km from the trench. The downdip limit of the 2004 rupture as inferred from aftershocks is within the 350° – 450° C temperature range, but this limit is 210–250 km from the trench axis and is much deeper than the fore-arc Moho. The deeper part of the rupture occurred along the contact between the mantle wedge and the downgoing plate.

Citation: Klingelhoefer, F., M.-A. Gutscher, S. Ladage, J.-X. Dessa, D. Graindorge, D. Franke, C. André, H. Permana, T. Yudistira, and A. Chauhan (2010), Limits of the seismogenic zone in the epicentral region of the 26 December 2004 great Sumatra-Andaman earthquake: Results from seismic refraction and wide-angle reflection surveys and thermal modeling, *J. Geophys. Res.*, *115*, B01304, doi:10.1029/2009JB006569.

1. Introduction

[2] Subduction megathrusts produce by far the largest earthquakes on Earth [Ruff and Kanamori, 1980; Stein and Okal, 2005]. These large ruptures also cause significant vertical motions that can generate devastating tsunamis

[Savage, 1983; Satake, 1993; Johnson *et al.*, 1996; Fujii and Satake, 2007]. Together these phenomena pose a substantial threat to populations and infrastructure located in coastal regions, such as most of the Pacific rim. The surface area of the earthquake fault plane, together with the amount of slip, controls the magnitude of the earthquake [Wells and Coppersmith, 1994]. The portion of the fault plane, which ruptures, is said to be “seismogenic” and is bounded by an updip and a downdip limit [Tichelaar and Ruff, 1993; Oleskevich *et al.*, 1999]. The position of the updip limit exerts a strong control on tsunami generation and the location of the downdip limit which commonly lies close to the coast, influences the intensity of ground shaking here. Therefore, it is of critical importance for the estimation and mitigation of these natural hazards to have reliable estimates of the updip and downdip limits. However, there is still no consensus on the physical processes which control these limits, and thus large uncertainties still exist for most zones which have not experienced a great earthquake in recent times, for example, Cascadia [Hyndman and Wang, 1995; Satake *et al.*, 1996; Khazaradze *et al.*, 1999; Stanley

¹Department of Marine Geosciences, Ifremer, Plouzané, France.

²UMR 6538, Domaines Océaniques, Université de Bretagne Occidentale, Institut Universitaire Européen de la Mer, Plouzané, France.

³Federal Institute for Geosciences and Natural Resources, Hanover, Germany.

⁴Géosciences Azur, UMR 6526, Observatoire Océanologique de Villefranche, Université Pierre et Marie Curie, CNRS, Villefranche sur Mer, France.

⁵Earth Dynamics and Geological Disaster Division, Research Center for Geotechnology, Indonesia Institute of Sciences, Bandung, Indonesia.

⁶Program Studi Teknik Geofisika, Institut Teknologi Bandung, Bandung, Indonesia.

⁷Laboratoire de Géosciences Marines, Institut de Physique du Globe de Paris, Paris, France.

and Villasenor, 2000]. This work focuses on the SE end of the rupture zone of the great Sumatra-Andaman earthquake of 26 December 2004, where the event initiated. We present new deep-penetration seismic data to constrain the geometry and structure of the crust and upper mantle. Additionally, numerical modeling of fore-arc thermal structure is performed in order to calculate the thermally expected limits of the seismogenic zone. These results are compared to the observed distribution of aftershocks and to published source-rupture models in order to determine where the earthquake rupture initiated. The implications for the control of seismogenic rupture by the lithologies and temperatures along the plate contact are discussed.

1.1. NW Sumatra Margin and the M9.3 2004 Earthquake

[3] One of the first deep seismic studies on the Sumatran subduction zone consisted of a two-ship survey in 1966–1967 [Curry *et al.*, 1977]. Their preferred interpretation of a profile off central Java shows minor thickening of the oceanic crust at the trench and slightly seaward which they propose to be caused by faulting. Later studies were carried out by Kieckhefer *et al.* [1980] using free floating sonobuoys, air guns and explosives on five margin-parallel lines located offshore Nias and in the Nias basin. On the basis of the analysis of this data set, they propose a shallow Moho depth beneath the continental crust of only about 20 km along this segment of the Sumatra fore arc.

[4] During the SUMENTA I and II cruises in 1992 over 5000 km of six-channel seismic data were acquired offshore Sumatra [Zart *et al.*, 1994], which helped to constrain the existence of the Mentawai microplate formed by partitioning of the oblique convergence of the subduction and strike-slip deformation of the upper plate [Malod and Kemal, 1996].

[5] More recent multichannel and wide-angle reflection seismic studies of the SE Sumatra to Java portion of the Sunda margin were carried out during the GINCO project with the German research vessel *Sonne* in 1998 and 1999. On the basis of these data, two main phases of fore-arc basin and accretionary prism evolution were identified [Schlüter *et al.*, 2002]. Analysis of the wide-angle data provided images of the subducting plate to a depth of 20 km and additionally the crustal structure was modeled to a depth of 30 km using gravity data [Kopp *et al.*, 2001]. Their preferred model includes a shallow Moho at only 15 km depth beneath the Java margin [Kopp *et al.*, 2002].

[6] The 26 December 2004 earthquake ($M_w = 9.1–9.3$) is among the four largest earthquakes ever recorded and the largest of the last 40 years [Lay *et al.*, 2005; Stein and Okal, 2005]. The earthquake initiated off the NW Sumatra margin in the vicinity of Simeulue Island, and ruptured northward past the Nicobar and Andaman islands, along 1300 km of the Indo-Australian–Sunda plate boundary [Lay *et al.*, 2005]. Source time studies [Ammon *et al.*, 2005] as well as geodetic [Vigny *et al.*, 2005] and tsunami data inversions [Fujii and Satake, 2007], indicate that the rupture zone was widest (up to 200 km), coseismic slip was largest (locally over 20 m) and thus seismic moment release was greatest, in the region directly west of the NW tip of Sumatra, near Banda Aceh (Figure 1).

[7] Several marine geophysical surveys were conducted after the earthquake on the Sumatran margin. During the

first cruise onboard the British military vessel HMS Scott multibeam bathymetry data were acquired on the southern part of the 2004 earthquake rupture zone [Henstock *et al.*, 2006]. From February–March 2005 a Japanese ocean bottom seismometer array was deployed to record the numerous aftershocks of the earthquake. The authors proposed the existence of two splay faults from the distribution of the earthquakes [Araki *et al.*, 2006]. During the French Aftershocks cruise, 20 ocean bottom seismometers (OBSs) were deployed in the region of largest slip offshore north-west of Sumatra. Examination of these data revealed the existence of two postseismic active thrust faults and two other thrust faults, which were not postseismically active [Sibuet *et al.*, 2007]. On the basis of the multibeam bathymetry data of the French and British cruises, it was proposed that the upper plate deformation is strongly influenced by the structure of the lower plate, which is characterized by north-south trending lineaments from the former Wharton spreading center [Graindorge *et al.*, 2008].

[8] Joint modeling of wide-angle and reflection seismic data from four profiles located offshore Simeulue acquired by the R/V *Sonne* in 2006 shows a significant deepening of the top of the oceanic crust toward the SE [Franke *et al.*, 2008]. The authors suggest that a ridge currently undergoing subduction in this region is responsible for the segmentation of the margin.

[9] The Sumatra-OBS geophysical survey was conducted in July–August 2006 onboard the R/V *Marion Dufresne* in this area. The objective was to determine the crustal structure in the epicentral region offshore NW Sumatra and in the zone of maximum coseismic displacement, some 300 km northward. We report here on the results of wide-angle seismic modeling of the Sumatra-AB profile, a transect across the epicentral region of the 26 December 2004 earthquake where the rupture initiated (Figure 2). Initial results from this survey are also reported by Dessa *et al.* [2009]. Further results from interpretation of reflection seismic profiles from a complementary cruise have been published recently [Singh *et al.*, 2008]. The authors interpret some deep reflections west of Simeulue Island as representing broken slices of oceanic crust, related to an oceanic mantle megathrust. They propose, that very strong coupling, appropriate for brittle failure of mantle rocks, accounts for the occurrence of the tsunamogenic event. Modeling of wide-angle and reflection seismic data on a profile north of Sumatra shows the presence of an active back thrust that is imaged down to at least 15 km depth and reaches the surface near the western edge of the Aceh fore-arc basin [Chauhan *et al.*, 2009]. The authors suggest that coseismic slip along the fore-arc back thrust boundary might provide an explanation for the generation of the tsunami.

[10] Modeling of the OBS data was performed in combination with the prestack depth migration of multichannel seismic data from the R/V *Sonne* cruise located close to the Sumatra-AB profile. Modeling of the limits of the seismogenic zone was undertaken using a geometry taken from both the multichannel and wide-angle seismic data.

1.2. Limits of the Seismogenic Zone

[11] Several decades of research have been devoted to understanding how the physical and mechanical properties of the rocks vary along the plate boundary fault plane and

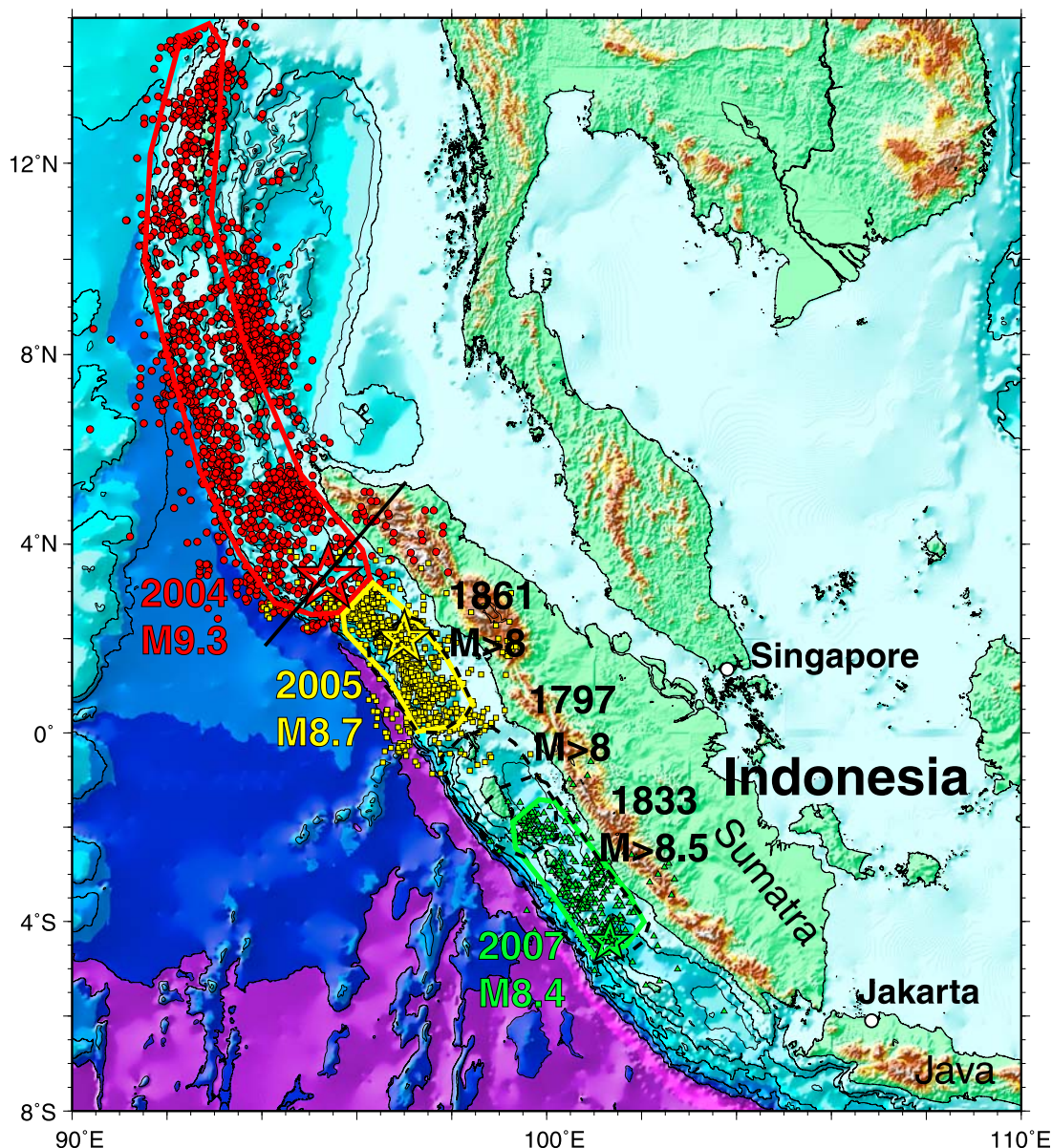


Figure 1. General location map of Sumatra convergent margin. The rupture planes of the three great earthquakes are shown, with the 3 month aftershocks in each case: $M9.3$, 26 December 2004 (red dots); $M8.7$, 28 March 2005 (yellow squares); and $M8.4$, 12 September 2007 (green triangles). The stars show where ruptures initiated. Estimated rupture zones from previous great earthquake sequences are shown as dashed lines [Lay *et al.*, 2005]. The location of the geophysical transect investigated in this study is indicated by the black line.

thus to try to answer the question, “Why are earthquakes generated here?” [Byrne *et al.*, 1988; Tichelaar and Ruff, 1993; Pacheco *et al.*, 1993; Oleskevich *et al.*, 1999]. A comprehensive review of current knowledge on the limits of the seismogenic zone is given by Hyndman [2007]. It has been suggested that the uppermost portion of the plate boundary, below the accretionary wedge behaves aseismically primarily due to the presence of high-porosity, fluid-rich sediments [Byrne *et al.*, 1988]. Whereas some margins have no accretionary wedge, in all cases it seems likely that the weakening effects of high fluid pressure within sediments along the plate interface can have an impact on

seismogenesis [Hubbert and Rubey, 1959; Davis *et al.*, 1983; Byrne and Fisher, 1990; Moore *et al.*, 1995; Saffer and Bekins, 2002]. Other studies on the updip limit proposed a possible control due to the rheological behavior of clay minerals and sediments as these undergo low-grade metamorphic reactions and diagenesis. In particular the opal to quartz and smectite to illite and chlorite transitions occur primarily over a temperature range of 100–150°C with the higher-grade minerals exhibiting a stick-slip rheology consistent with seismogenic behavior [Vrolijk, 1990; Moore and Saffer, 2001]. However, recent laboratory studies are inconsistent at least for the experimental range of conditions

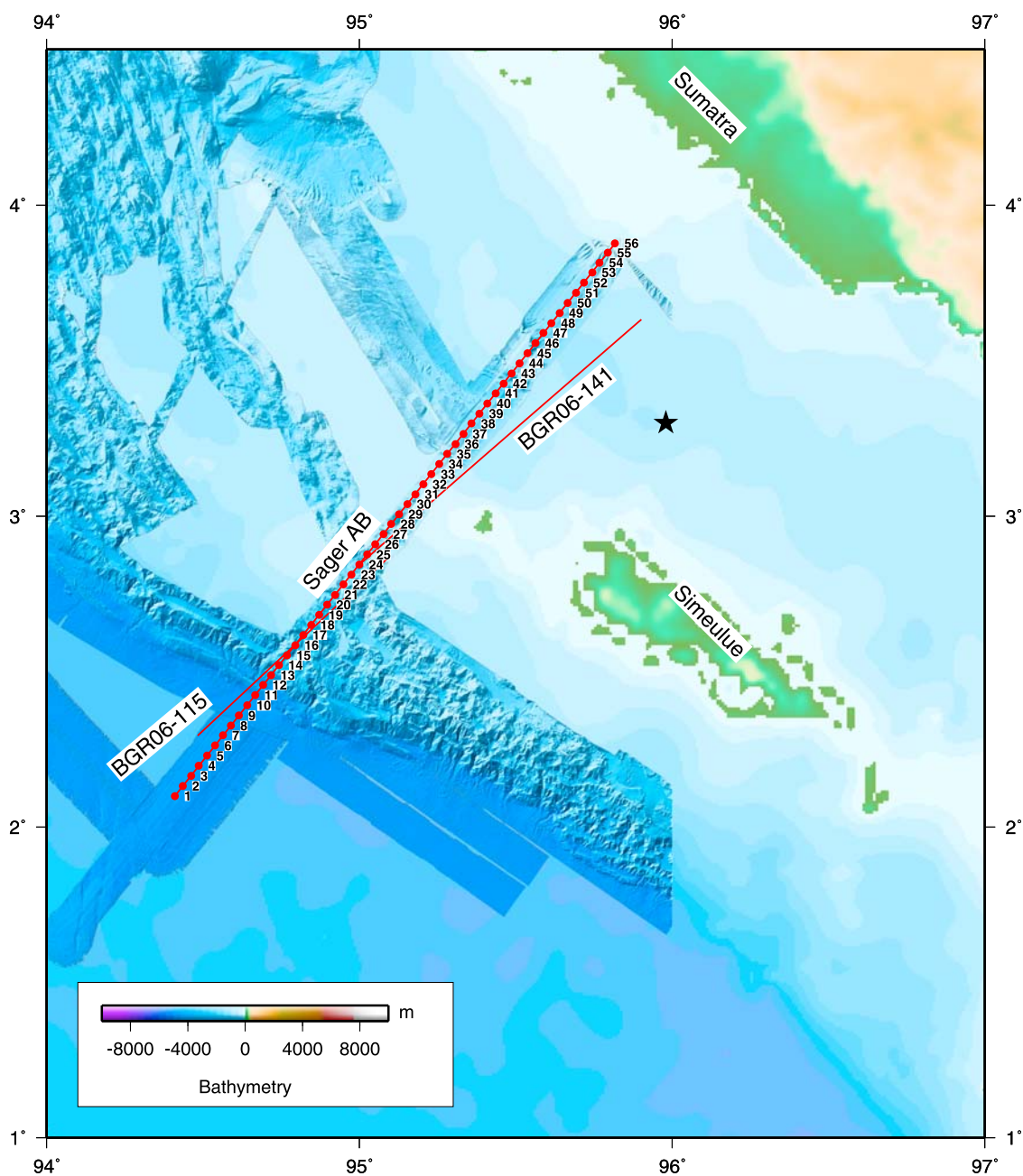


Figure 2. Seafloor bathymetry of the study region from Aftershocks and Sumatra-OBS cruises. OBSs are marked by red dots, and multichannel seismic profiles are marked by red lines. Shaded areas are not covered by shipboard-measured bathymetry and show predicted bathymetry from satellite altimetry [Sandwell and Smith, 1995]. The star marks the location of the great Sumatra earthquake.

tested, with the smectite-illite transition being the sole control on the updip limit of the seismogenic zone [Marone and Saffer, 2007].

[12] There is also discussion on the mechanisms controlling the downdip limit. The two propositions are a thermal control due to the transition to dislocation creep at high temperatures [Scholz, 1990; Hyndman and Wang, 1993] or alternatively, that the presence of a highly serpentinized mantle wedge, which permits aseismic sliding, may define the downdip limit of seismogenic behavior [Hyndman et al., 1997]. A global analysis of subduction megathrust earthquakes indicates that on average, the downdip limit occurs

at a depth of 40 ± 5 km [Tichelaar and Ruff, 1993] though some subduction zones may have shallower downdip limits of about 20–30 km, such as Mexico [Currie et al., 2002] and Cascadia [Hyndman and Wang, 1995; Gutscher and Peacock, 2003]. This depth range could potentially correspond to either a thermal control or to a serpentinized mantle wedge, depending on the geometry and lithology of the margin in question.

[13] For most well-studied margins (SW Japan, Cascadia, Chile, Mexico, and Alaska), there seems to be a fairly good agreement between the thermally predicted updip and downdip limits, and these limits as obtained from other

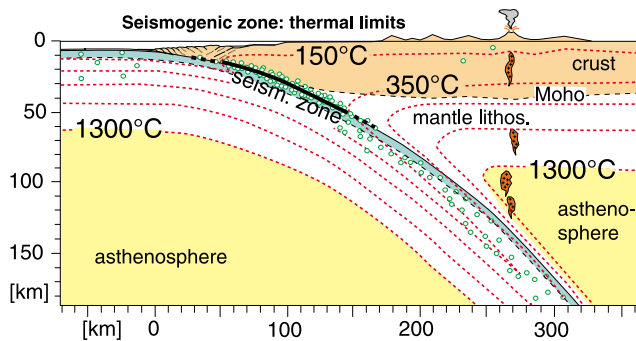


Figure 3. Schematic representation of a subduction zone showing the seismogenic zone where stick-slip behavior is believed to occur between the 150°C and 350°C isotherms. Note that transition zones exist (dashed lines) above the updip limit to around 100°C and below the downdip limit to around 450°C (see text for further explanation).

methods (e.g., source time studies, aftershock studies, geodetic studies, and tsunami modeling) [Hyndman *et al.*, 1995; Hyndman and Wang, 1995; Oleskevich *et al.*, 1999; Currie *et al.*, 2002; Gutscher and Peacock, 2003] (Figure 3). Thus, thermal modeling appears to be a very useful method for determining the position of both the updip and downdip limit.

2. Multichannel Seismic Reflection Data

[14] During a multichannel seismic (MCS) survey with the German R/V *Sonne* in January–February 2006 a comprehensive data set of 5358 kilometers of MCS data was acquired coincident with gravity and magnetics in Indonesian waters over the southern part of the 2004 and the 2005 rupture zones [Ladage *et al.*, 2006]. We used a 240 channel, 3 km streamer, and a tuned air gun array consisting of 16 air guns with a total capacity of 50.8 L. Record length was 14 s with a sample interval of 2 ms.

[15] Processing of the two MCS lines BGR06-115 and BGR06-141 was performed up to full Kirchhoff prestack depth migration and included the production and correction via MVA (migration velocity analysis) of a depth velocity model. After testing various combinations of processing parameters the following sequence was regarded as optimal. Prestack processing included geometry editing, deconvolution, true amplitude recovery, and time and space variant signal filtering. Reduction of water-bottom multiples was achieved by applying a parabolic radon filter and inner trace mutes. Stacking velocities, at an average distance interval of 3 km, were determined for the reference poststack time-migrated sections. The initial depth model was derived by combining the velocity field from the smoothed stacking velocities (upper section) with the wide-angle/refraction seismic data from the AB profile located close to these profiles along the lines BGR06-115 and BGR06-141 for the lower section. Particularly, the upper parts of the velocity fields were iteratively improved via MVA until the migrated CRP (common reflection point) gathers were flat. Quality control included a detailed evaluation of congruence between the poststack migrated sections and the time-converted prestack depth-migrated sections.

[16] The MCS data were used to constrain the shallow crustal structure in the trench region and the frontal portion of the accretionary wedge. Profile BGR06-115 images the thick undeformed sedimentary section (3 s TWT) at the trench and the accretionary wedge (Figure 4). The major reflectors observed were used to help construct the p wave velocity model based on the OBS data. For the thermal modeling described below it was also particularly important to obtain the position of the deformation front, the sediment thickness above the decollement and the geometry (depth and dip) of the decollement fault plane, which represents the plate boundary fault.

3. Wide-Angle Seismic Data

[17] Wide-angle seismic data were processed using a tomographic approach to obtain an independent velocity model [Zelt and Barton, 1998], followed by forward modeling in order to incorporate secondary arrivals and the main reflectors from the reflection seismic data [Zelt and Smith, 1992]. Error analysis included calculation of synthetic seismograms, in order to constrain velocity gradients, and gravity modeling.

3.1. OBS Data Acquisition and Quality

[18] During the Sumatra-OBS cruise (R/V *Marion Dufresne*, July–August 2006) 56 ocean bottom seismometers from the British OBIC pool, the French INSU pool, the University of Brest and Ifremer were deployed along the above mentioned SW–NE oriented Sumatra-AB profile just north of Simeulue Island, in the epicentral area (Figure 2). The profile is 252 km long, resulting in a 4.6 km instrument spacing. All instruments were successfully recovered. A total of 2090 shots were fired on the profile by a 8260 m³ air gun array tuned to single-bubble mode to enhance the low frequencies and allow deep penetration [Avedik *et al.*, 1993]. Preprocessing of the OBS data included calculation of the clock-drift corrections to adjust the clock in each instrument to the GPS base time. Instrument locations were corrected for drift from the deployment position during their descent to the seafloor using the direct water wave arrival. The drift of the instruments never exceeded 100 m. Picking of the onset of first and secondary arrivals was performed semi-automatic with a manual quality control and without filtering where possible.

[19] Data quality along the profile is generally good on all channels, although some instruments show bands of noise on their geophone probably due to water currents. Instruments deployed without a trailing buoy displayed lower noise levels. The OBSs located on oceanic crust show very good data quality (Figure 5) with clear arrivals from the sedimentary layers, crust, and upper mantle. Toward the toe of the accretionary prism, the OBS data sections show an increasing amount of sedimentary arrivals (Figure 6). On the accretionary wedge the data sections are highly asymmetric and display long and partly disturbed sedimentary arrivals (Figure 7). Those instruments located in the fore-arc basin are mostly characterized by clear sedimentary phases as well as reflections from the base of the top and base of oceanic crust. Data sections from the most landward OBSs on the profile allow us to identify reflected arrivals from the

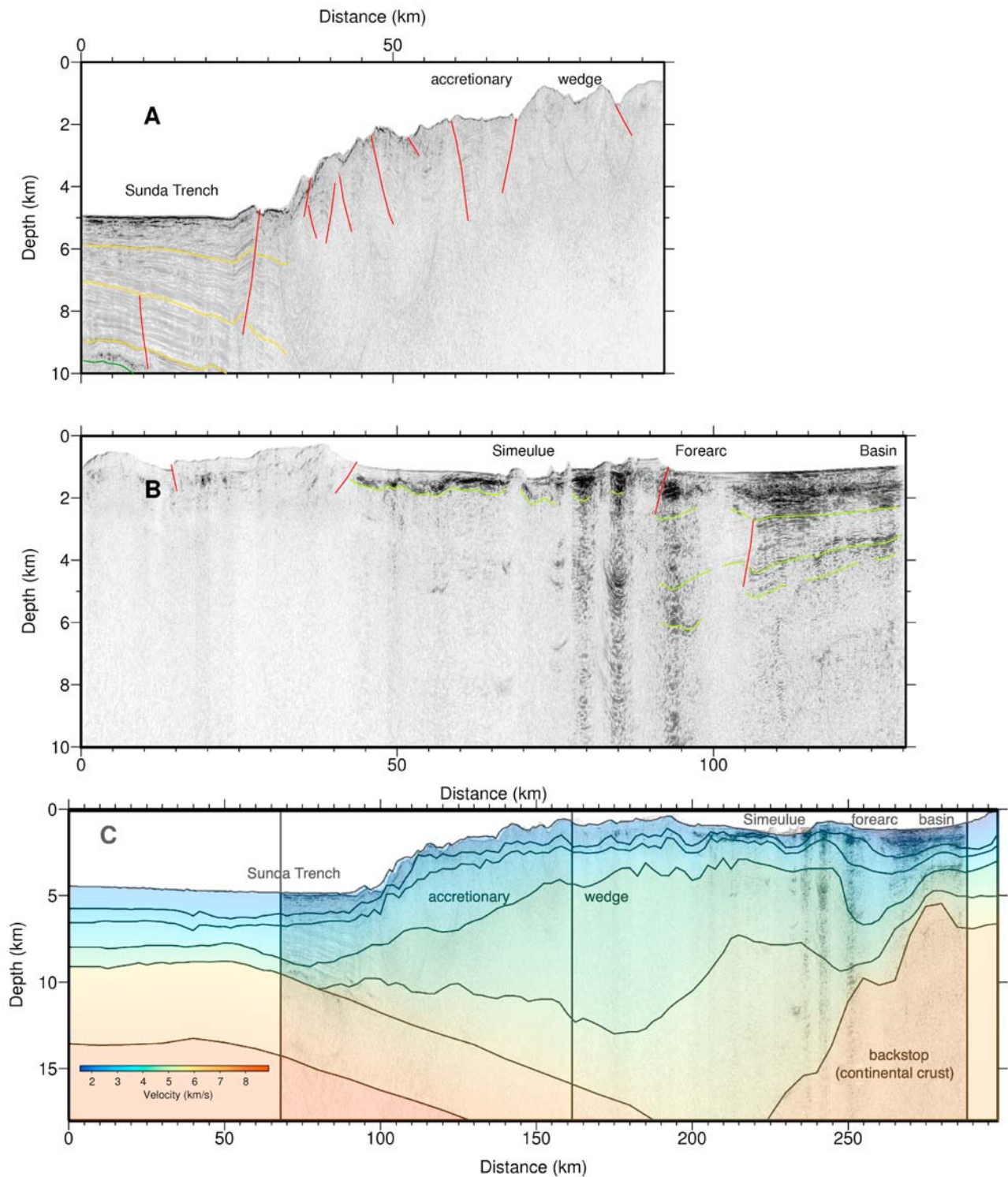


Figure 4. Multichannel reflection seismic profiles from the Bundesanstalt für Geowissenschaften und Rohstoffe (BGR) SeaCause II cruise in 2006. (a) Prestack depth-migrated section of profile BGR06-115, (b) prestack depth-migrated section of profile BGR06-141, and (c) profiles BGR06-115 and BGR-141 with layer boundaries and velocities from the wide-angle seismic modeling overlain.

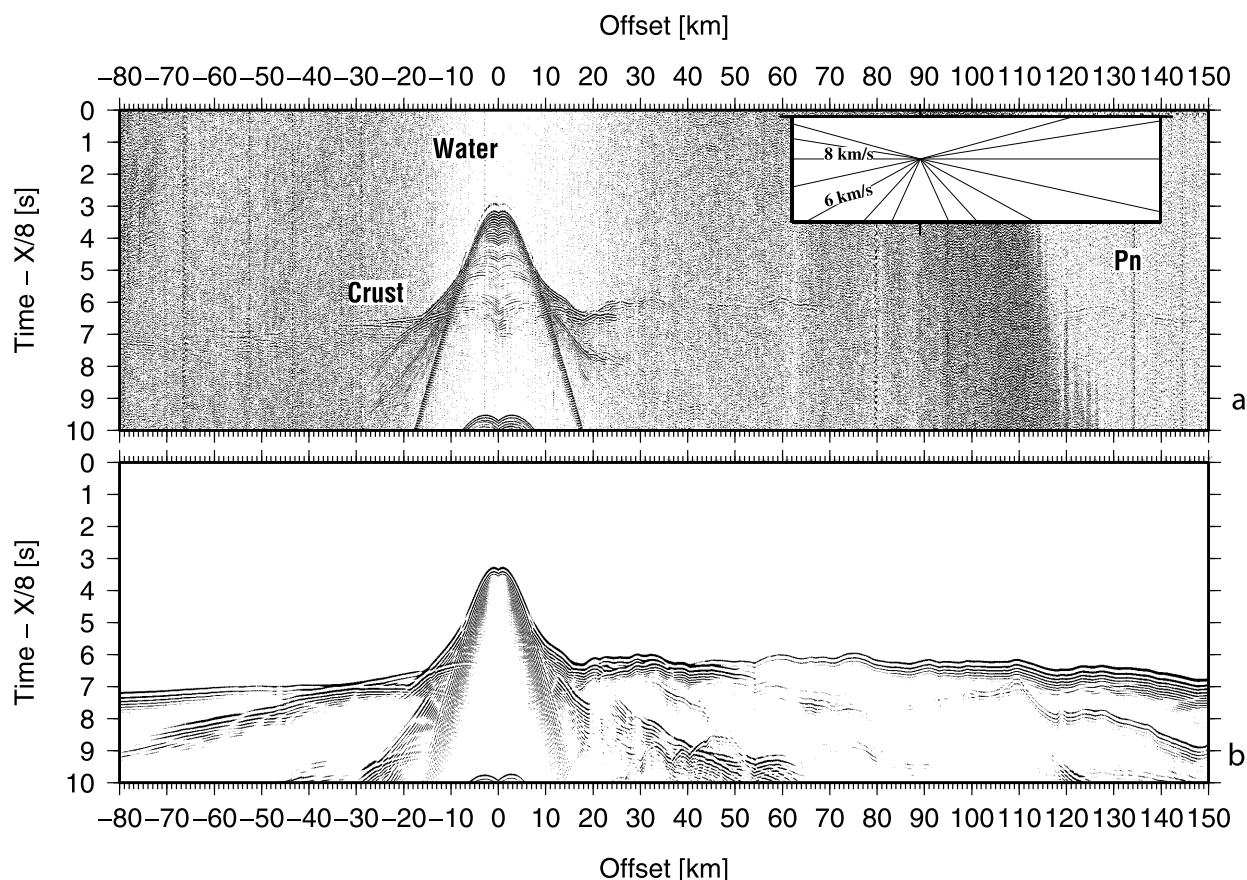


Figure 5. (a) Band-pass-filtered (3–5 Hz, 24–36 Hz) vertical geophone data section from OBS 05 located on oceanic crust. The data are displayed with a gain proportional to source-receiver offset and are reduced at a velocity of 8 km/s. *PmP* (reflection from the Moho) and *Pn* (turning waves from the upper mantle) are annotated. (b) Synthetic seismograms calculated from the velocity model for the same station using the finite difference modeling code from the Seismic Unix package [Cohen and Stockwell, 2003; Stockwell, 1999]. The synthetic seismograms are calculated every 100 m with a source frequency centered around 8 Hz.

base of the continental crust as well as the base of the oceanic crust that subducts below (Figure 8).

3.2. Tomographic Inversion

[20] The tomographic inversion code FAST [Zelt and Barton, 1998] was used to constrain a velocity distribution that was used as an initial guideline to the forward modeling, described hereafter. This code uses a regularized inversion in which the user can specify parameters for the travel time misfit and model roughness of the final solution. The method is linearized in that a starting model and iterative convergence scheme are employed. Nonlinearity is accounted for by calculating new raypaths for each iteration. The method generates smooth models, which do not resolve sharp boundaries but steeper velocity gradients instead. The most important structural features are thus resolved in an objective manner, that is, not user-oriented. Similar tomographic inversion methods have been used in previous studies to constrain the crustal and upper mantle velocities in subduction zones [e.g., Graindorge et al., 2003; Dessa et al., 2004; Ramachandran et al., 2006; Gailler et al., 2007].

[21] In order to perform this tomographic inversion of the first arrivals, 33,127 travel times have been picked in the complete data set. Each pick has been assigned a picking error between 20 ms and 150 ms depending on the data quality. The tomographic model used a grid of 320 km × 40 km with a 1 km grid cell size (Figure 9). For the final model run, five different smoothing weights were tested in 10 nonlinear iterative steps. The final model predicts a mean travel time misfit of 156 ms. 97% of all picks were traced in the model.

3.3. Forward Ray-Tracing Modeling

[22] To be able to include reflections from the oceanic and continental crust into the modeling process, we converted the tomographic model into a forward ray-tracing model using the RAYINVR software [Zelt and Smith, 1992] (Figure 10). The number of picks used for the forward modeling was 36,322, about 3200 picks higher than the tomographic model. Sedimentary layers were taken from isovelocity contours of the inversion model and from reflection seismic data of the region of the model. Crustal layers and the Moho were modeled using phases generated

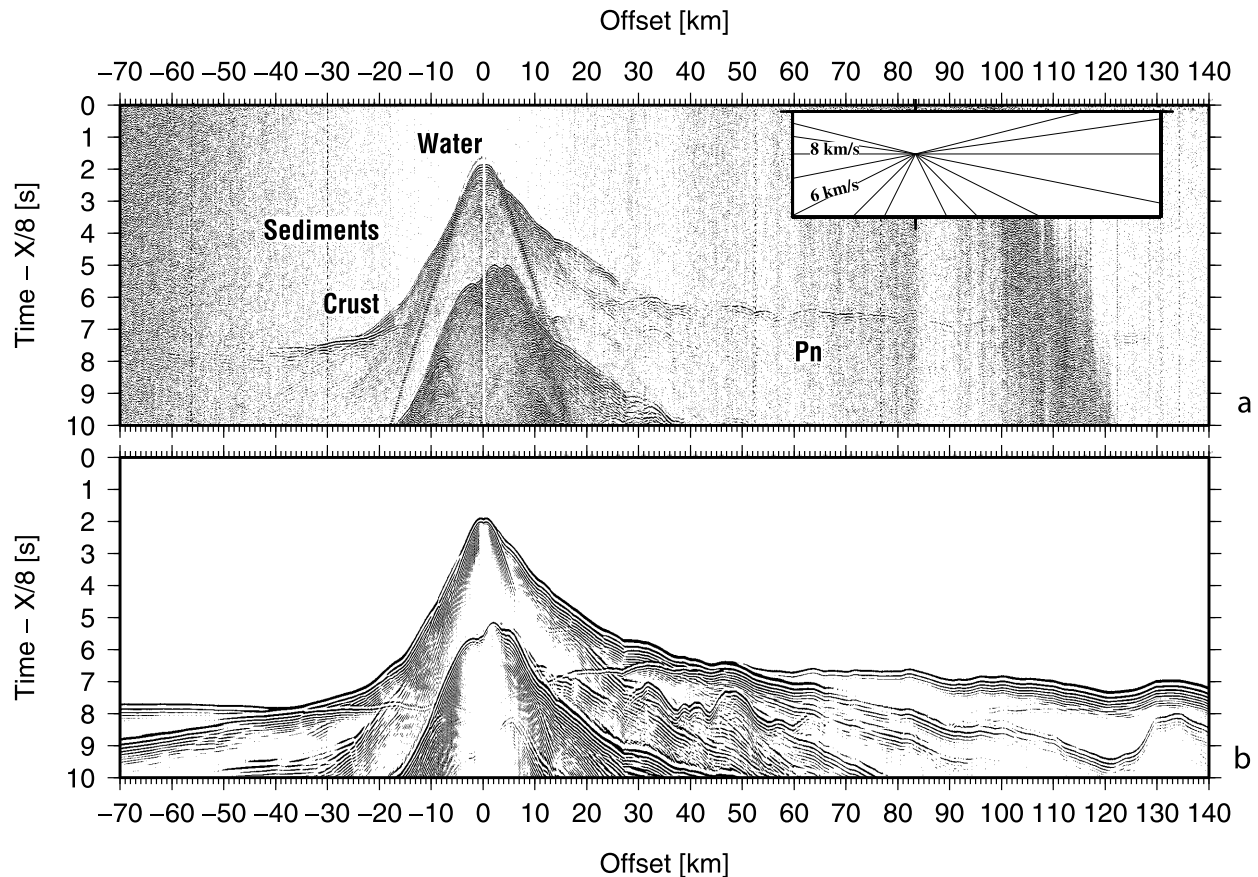


Figure 6. (a) Data from the vertical geophone data section from OBS 11 located on oceanic crust close to the accretionary prism. The gain, filter, and scaling are the same as those applied in Figure 5a. (b) Corresponding synthetic seismograms calculated from the model using the same method as that in Figure 5b.

by diving waves and deep reflected phases. This was done in accordance with the tomographic model. For the model parameterization, we used the minimum-parameter/minimum-structure approach, to avoid inclusion of velocity or structural features into the model unconstrained by the data [Zelt, 1999]. Velocity gradients and phase identification in the velocity model were further constrained by synthetic seismogram modeling using the finite difference modeling code from the Seismic Unix package [Cohen and Stockwell, 2003; Stockwell, 1999] (Figures 5b, 6b, 7b, and 8b).

3.4. Error Analysis

[23] In order to constrain the dependency of the final tomographic model on the initial model and especially the robustness of the high-velocity zone interpreted to be the mantle wedge, which is located at the boundary of the model, different model runs were conducted using different initial models. A variety of simple initial models were selected and the inversion performed (Figure 11). The resulting models are characterized by a lower fit of the data. Nevertheless the high-velocity anomaly is found in all resulting models, even though the exact location and amplitude do vary. One test run with high velocities at unrealistically low depths underneath the continental crusts produced a velocity anomaly more shallow (15 km depth) than our preferred final model.

[24] Two-point ray tracing between source and receiver (Figure 12) shows the well-resolved and the unconstrained areas. Ray coverage for diving and reflected waves is generally very good due to the excellent data quality and close instrument spacing (Figures 12a and 12b). All sedimentary layers are well sampled by reflected and turning rays in the model. The crustal layers are well sampled except for the oceanic crust of the subducted slab at depth larger than 30 km. The oceanic Moho at depth greater than 30 km, the continental Moho and the mantle wedge geometry are mainly constrained by reflected arrivals, which generally produce higher-amplitude arrivals than diving waves from layers of low seismic velocity gradients such as the upper mantle. The Moho has been additionally constrained by gravity modeling at the ends of the profiles. The fit between predicted arrival times and travel time picks provides information about the quality of the model (Figure 12). The corresponding misfit is 0.125 s using 95% of the picks.

[25] Construction of a tomographic model as well as a forward ray-tracing model allows us on the one hand to include additional information from the reflected phases and the multichannel data into the model and on the other hand to verify that all structures from the forward model are required to fit the data. These models are therefore complementary and help to support our conclusions.

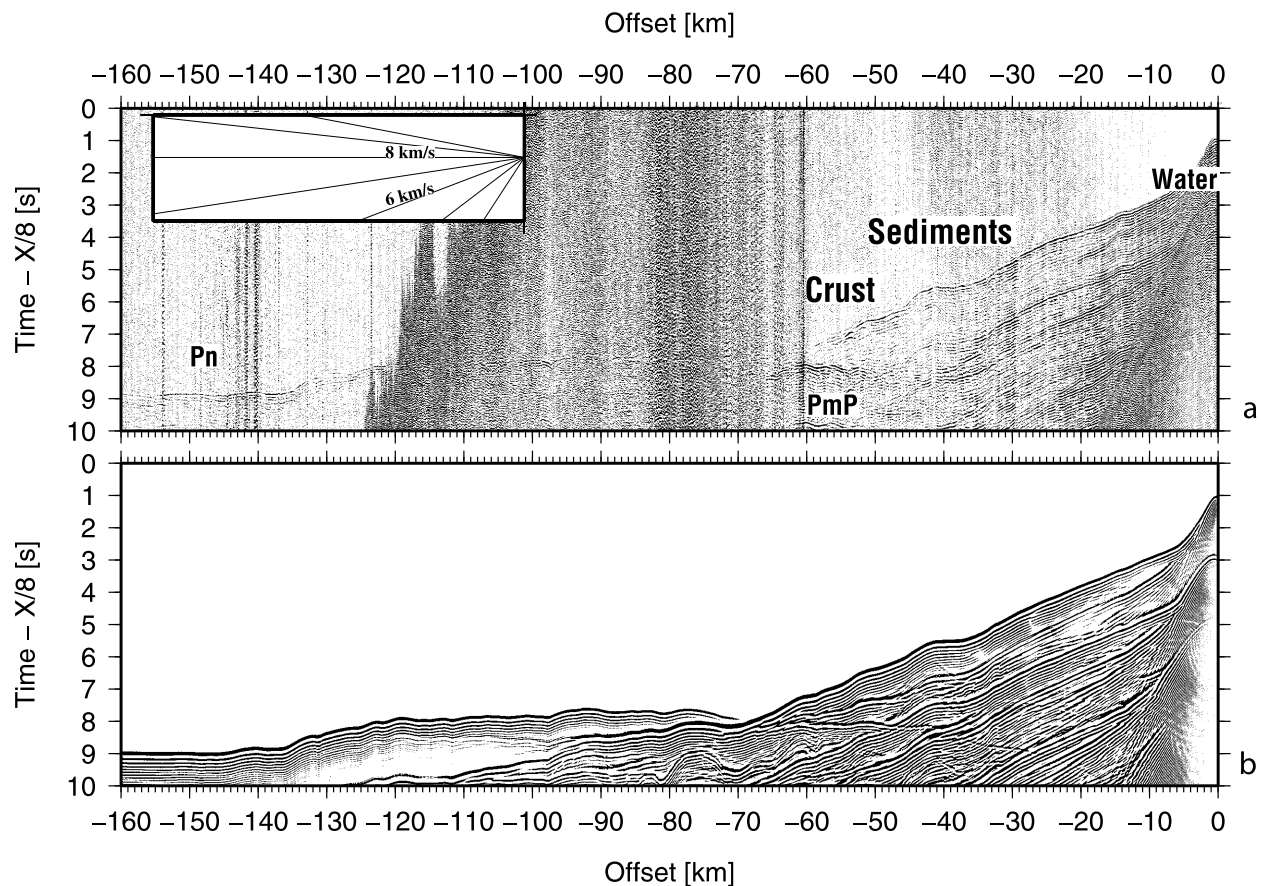


Figure 7. (a) Data from the vertical geophone data section from OBS 34 located on the accretionary prism. The gain, filter, and scaling are the same as those applied in Figure 5a. (b) Corresponding synthetic seismograms calculated from the model using the same method as that in Figure 5b.

[26] As the correct identification of velocity anomalies and the degree of resolution of the model are of fundamental interest to the conclusions of the work, additional calculations of the velocity resolution and depth uncertainty have been performed. The quality of the velocities in the model can be estimated from the resolution parameter (see Figure 13). Resolution is a measure of the number of rays passing through a region of the model constrained by a particular velocity node and is therefore dependent on the node spacing [Zelt, 1999]. If a layer can be modeled with one single velocity gradient the resolution parameter will be high even in areas which have lower ray coverage as the area is related to only one velocity node. Nodes with values greater than 0.5 are considered well resolved (Figure 13). In order to estimate the velocity and depth uncertainty of the final velocity model a perturbation analysis was performed. The depths of key interfaces were varied and an F test was applied to determine if a significant change between models could be detected. The 95% confidence limit gives an estimate of the depth uncertainty of the interface (Figure 13). The sedimentary and crustal layers are well constrained throughout the model. The velocities in the mantle wedge show a resolution of between 0.3 and 0.7 due to the missing information from turning rays in this layer. The upper mantle velocities are well constrained. At greater depth the velocities are less constrained due to fewer rays penetrating into this deeper portion of the model. The depth of

the main depth interfaces is constrained to a depth error of about ± 1 km.

[27] In order to constrain the velocity gradients of the different layers, synthetic seismograms were calculated and compared to the data sections. The finite difference modeling code from the Seismic Unix package [Cohen and Stockwell, 2003; Stockwell, 1999] was used to calculate synthetic seismograms of a record length of 30 s at a 100 m spacing (Figures 5b, 6b, 7b, and 8b). The program uses the explicit second-order differencing method for modeling the acoustic wave equation. The input velocity model was calculated from sampling the forward velocity model at a lateral 50 m interval and 10 m interval in depth. In order to avoid grid dispersion, the peak frequency of the Ricker wavelet source signal is calculated to be equal to the lowest velocity of the medium divided by the grid points per wavelength multiplied by 10. In this case the source wavelet is centered at 8 Hz, similar to the signal from the air gun array used during the cruise. The boundary conditions were set to be absorbing at the sides and bottom of the model and free at the surface. Detailed ray coverage, travel time fit, and synthetic data provide additional information of the identification of the picked phases (Figures 14 and 15).

3.5. Gravity Modeling

[28] Since seismic velocities and densities are well correlated, gravity modeling provides an important additional

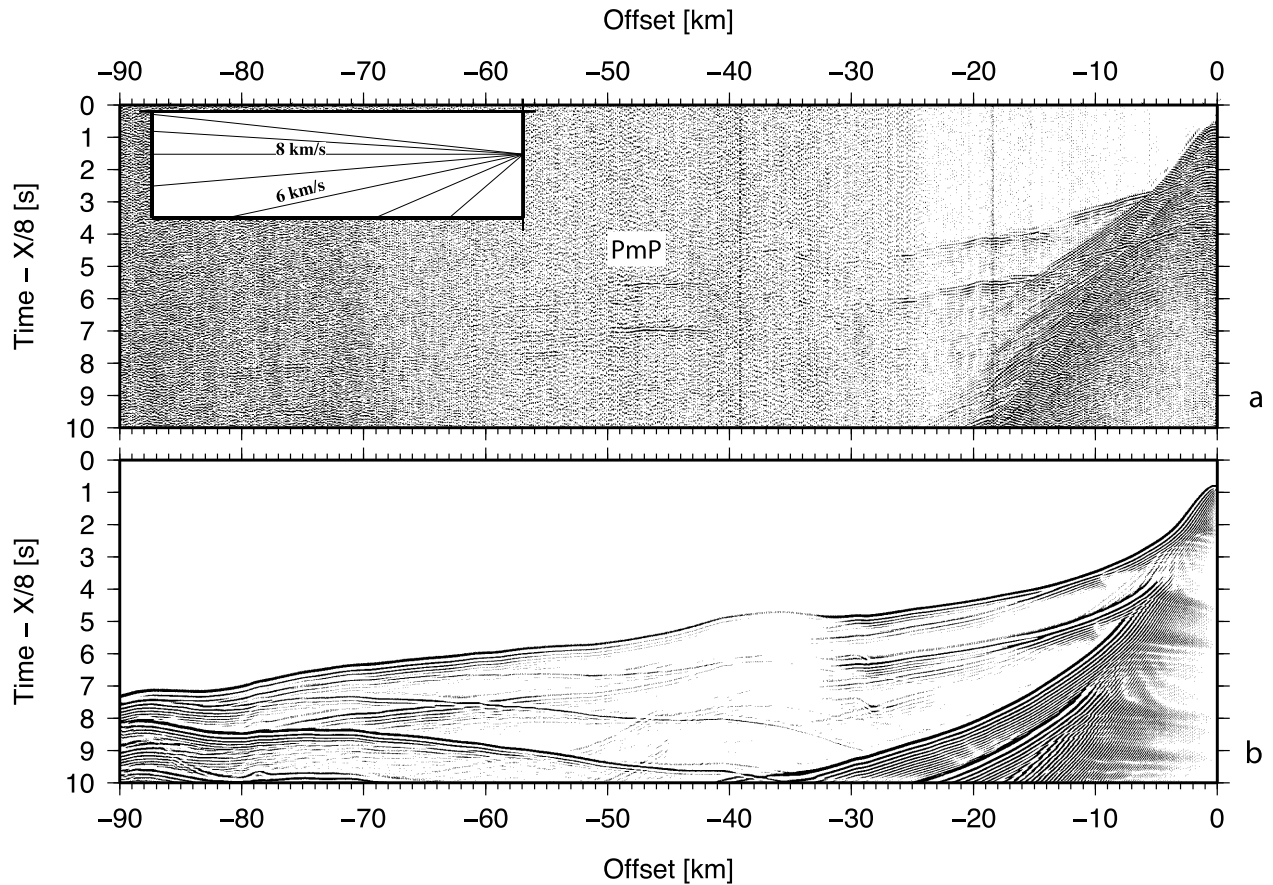


Figure 8. (a) Data from the vertical geophone data section from OBS 44 located the end of the profile. The gain, filter, and scaling are the same as those applied in Figure 5a. (b) Corresponding synthetic seismograms calculated from the model using the same method as that in Figure 5b.

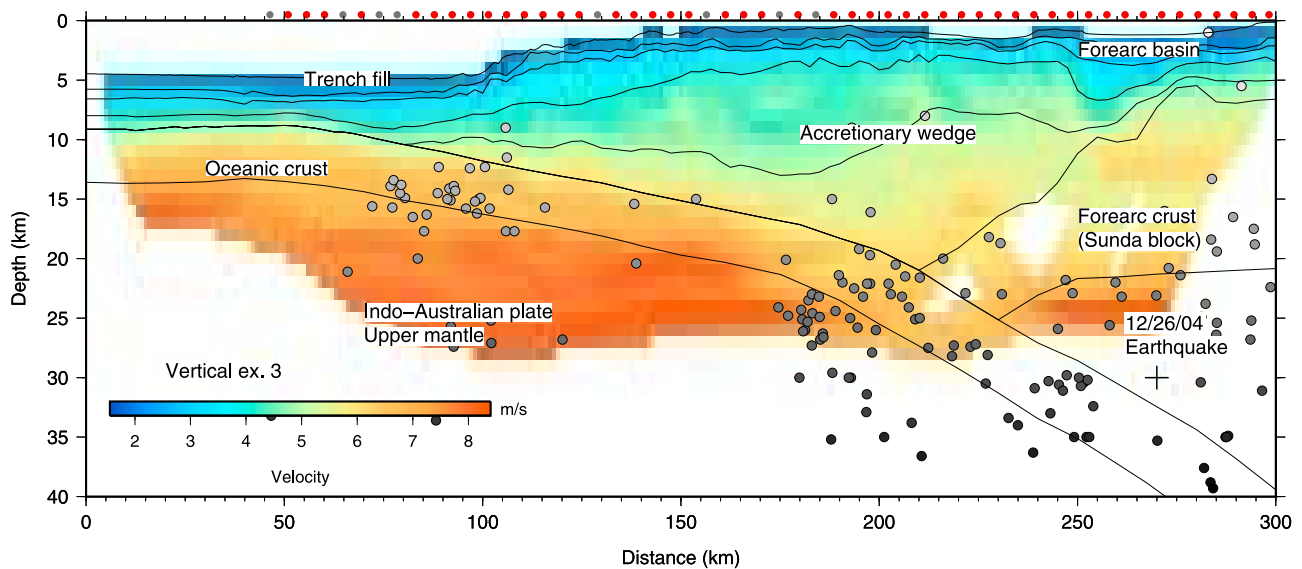


Figure 9. Result of the tomographic inversion of first arrivals. Black lines represent layer boundaries from forward modeling. Dots mark aftershock locations [Engdahl *et al.*, 2007]. The hypocenter of the 2004 earthquake is projected onto the model and marked by a cross.

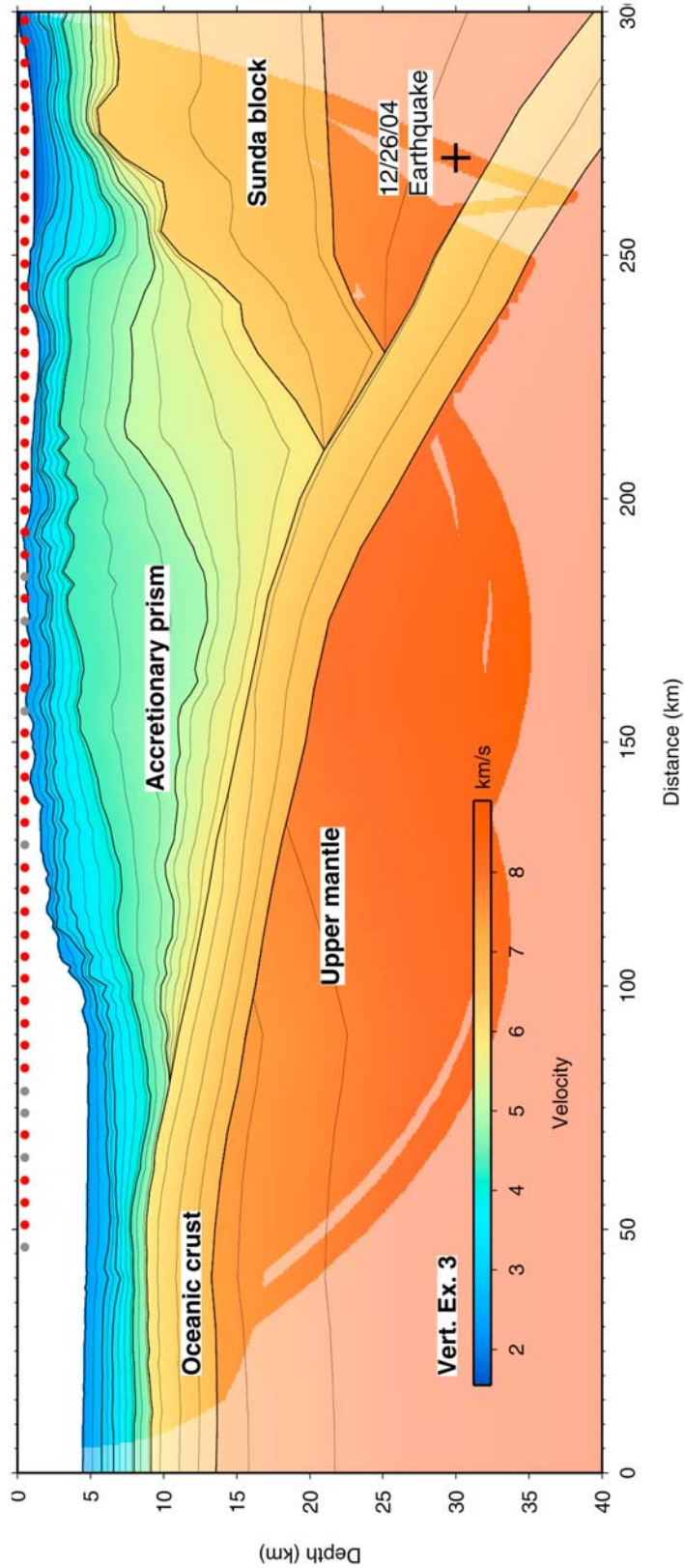


Figure 10. Final velocity models for the profile, including the model boundaries used during inversion (solid lines) and isovelocity contours every 0.25 km/s. OBS locations are indicated by red dots. Areas unconstrained by ray-tracing modeling are shaded. Vertical exaggeration is 3 times.

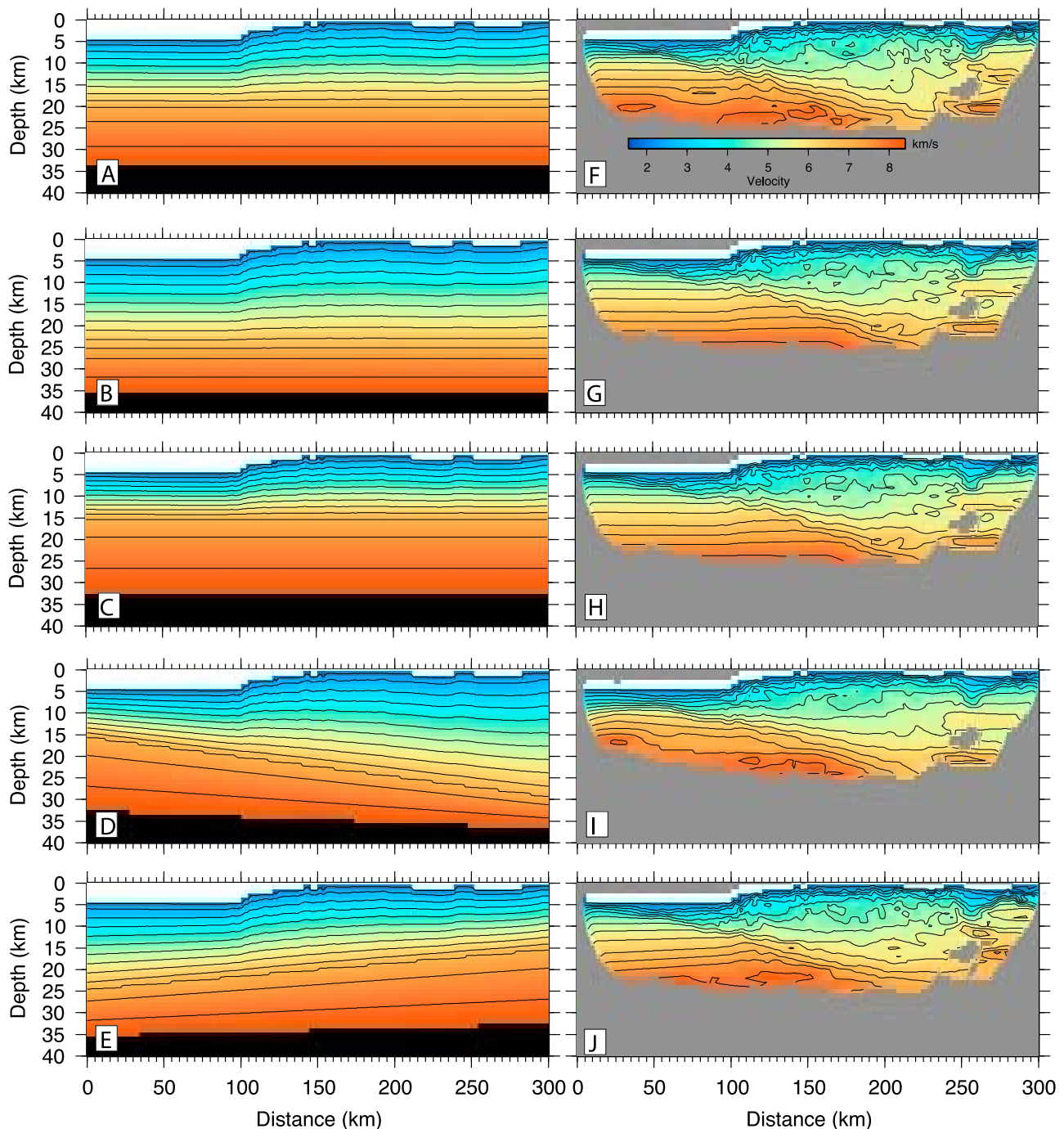


Figure 11. Variation of the starting model. (a) Initial model as used in this study. (b) Initial model with a 5 km lower crust-mantle boundary. (c) Initial model with a 5 km higher crust-mantle boundary. (d) Initial model with a strong slope dipping toward the continent in the crust-mantle boundary. (e) Initial model with a strong slope dipping toward the oceanic plate in the crust-mantle boundary. (f) Velocity model resulting from Figure 11a, leading to a $ch^2 = 9.8$. (g) Velocity model resulting from Figure 11b, leading to a $ch^2 = 20.25$. (h) Velocity model resulting from Figure 11c, leading to a $ch^2 = 11.5$. (i) Velocity model resulting from Figure 11d, leading to a $ch^2 = 14.7$. (j) Velocity model resulting from Figure 11e, leading to a $ch^2 = 12.6$.

constraint on the seismic model. Areas unconstrained by the seismic data can be modeled by comparing calculated gravity anomalies with those observed.

[29] The gravity data were forward modeled using the gravity module of the software of *Zelt and Smith* [1992].

Average P wave velocities for each layer of the seismic models were converted to densities in good agreement with different velocity density relationships from laboratory measurements [*Ludwig et al.*, 1970; *Carlson and Herrick*, 1990; *Hughes et al.*, 1998; *Hamilton*, 1978] for the sedi-

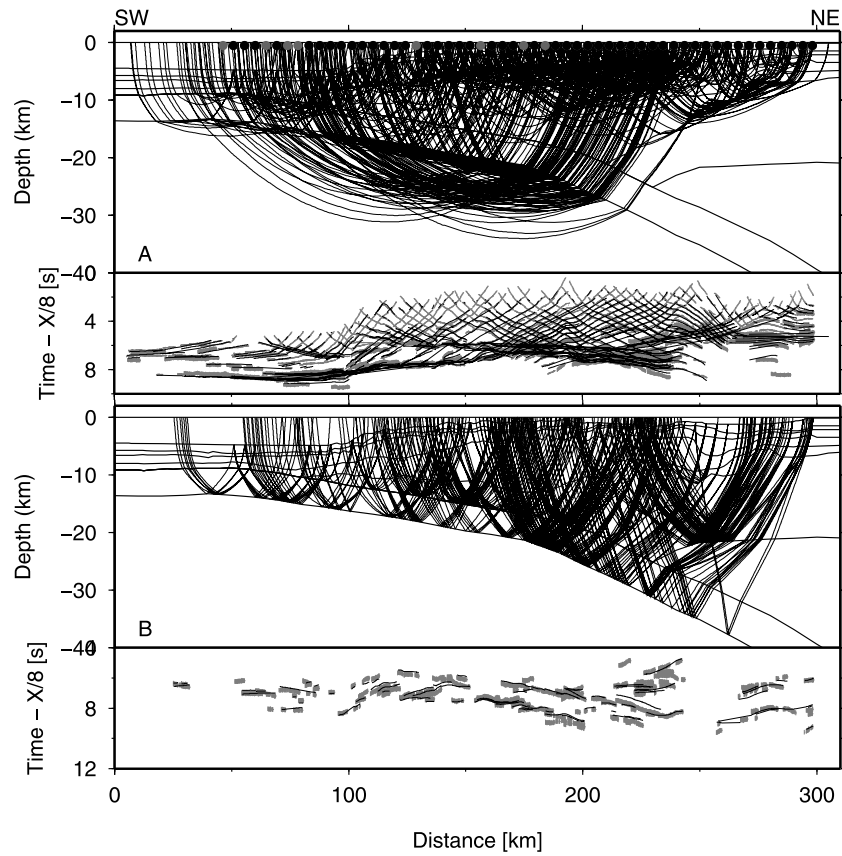


Figure 12. (a) Ray coverage of diving waves with every fortieth ray from two-point ray-tracing plotted at top and observed travel time picks and calculated travel times (lines) for the same phases for all receivers along the model plotted at bottom. (b) Same as Figure 12a but for reflected phases.

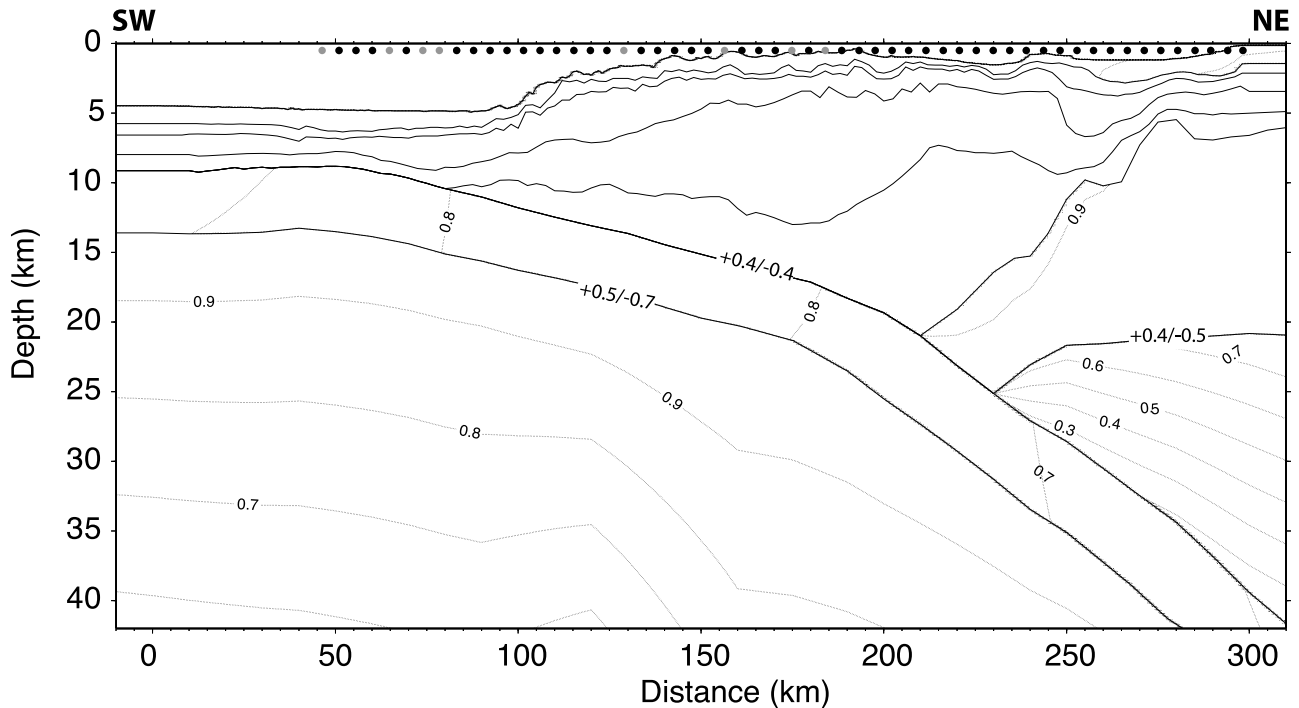


Figure 13. Resolution parameter for depth nodes of the velocity model. Contour interval is 0.1. The depth uncertainty of the most important boundaries calculated from the 95% confidence limit of the F test is annotated for the main reflectors.

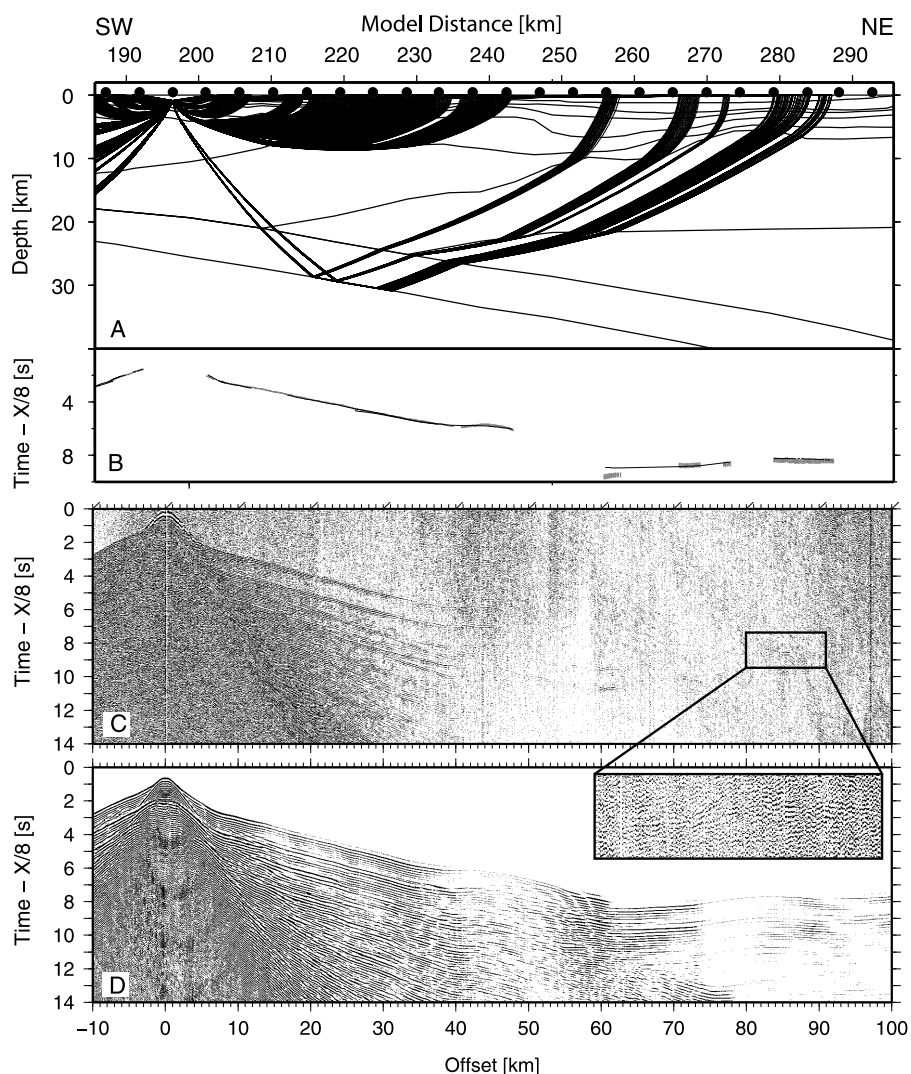


Figure 14. (a) Ray coverage of OBS 26 in the model, (b) travel time fit of the associated rays, (c) data section corresponding to the model, and (d) synthetic seismograms corresponding to the model.

mentary layers and the relationship of *Christensen and Mooney* [1995] for crustal layers (Figure 16). Layers from the velocity modeling have only been subdivided where necessary and strong lateral velocity gradients are present. The upper mantle densities were set to a constant 3.32 g/cm^3 . To optimize the fit of the final gravity model (Figure 17) the densities of each layer were subsequently manually varied within an error bound of 0.25 km/s from their original value. This deviation is considered a realistic uncertainty of empirical relationships used for the velocity-density conversion. To avoid edge effects both models were extended by 100 km at both ends and down to a depth of 95 km . The calculated anomalies can be compared with the shipboard measured gravity anomaly (Figure 17). The predicted anomalies generally fit the observed data well. The largest misfit is observed at around 240 km model distance and might be caused by three-dimensional effects of the base-tent topography.

[30] For comparison we have calculated two additional models, in which the mantle wedge is replaced by either continental crustal material, with a density of 2.83 kg/m^3 or normal upper mantle material characterized by a density of

3.32 kg/m^3 (Figure 17). Neither of the two alternative models shows a fit as satisfactory as our preferred model with a density of 3.1 kg/m^3 .

4. Numerical Modeling of the Sumatra Fore-Arc Thermal Structure

[31] We applied finite element modeling of the fore-arc thermal structure in order to determine the temperature distribution along the plate interface and to predict the updip and downdip limits of the seismogenic zone. This approach is based on models, which consider temperature (together with lithology) as one of the primary controls of stick-slip rheological behavior that lead to earthquake rupture [Hyndman and Wang, 1993; Hyndman et al., 1997; Peacock and Wang, 1999; Gutscher and Peacock, 2003] (Figure 2). The geometry of the subducting oceanic crust and the upper plate (down to $20\text{--}30 \text{ km}$ depth) is constrained primarily by the OBS data presented above. The total sedimentary thickness of 5 km at the trench and a decollement at 4 km depth are taken from published seismic reflection data [Karig et al., 1980; Singh et al., 2008] and

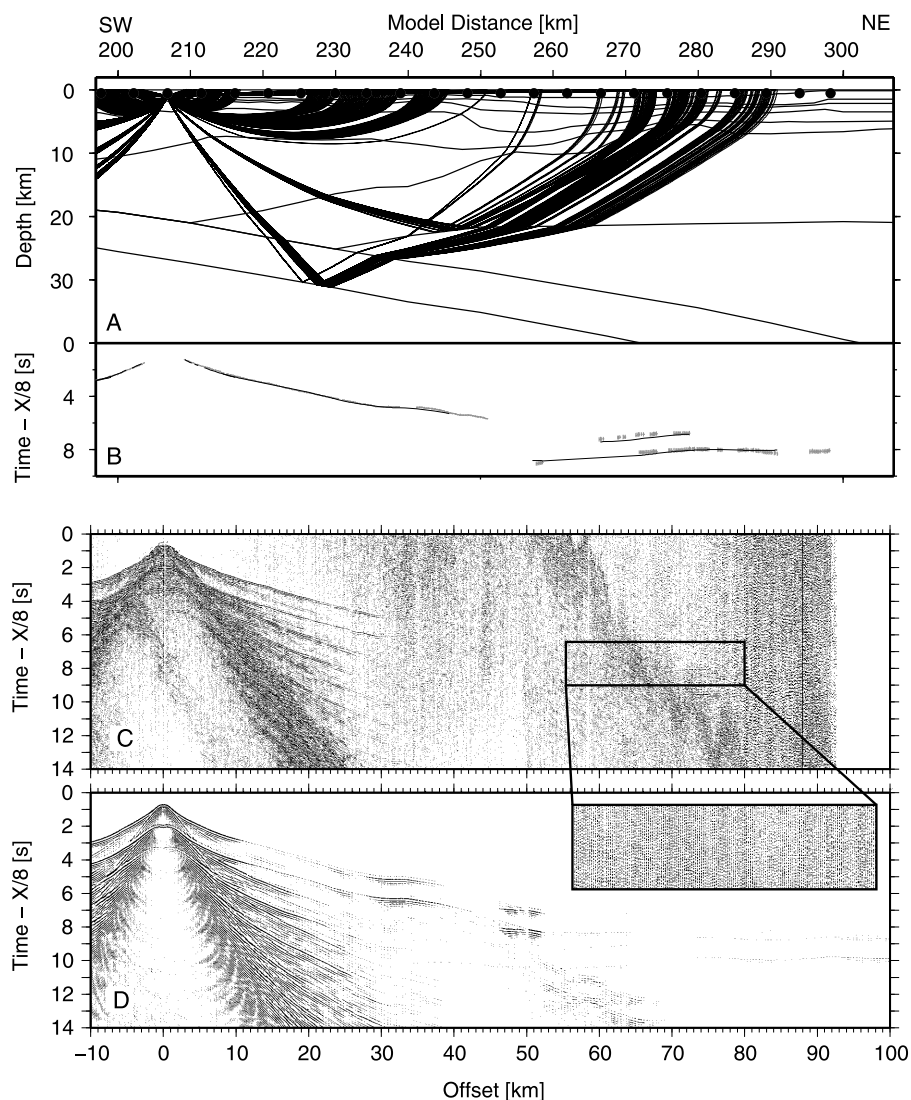


Figure 15. (a) Ray coverage of OBS 28 in the model, (b) travel time fit of the associated rays, (c) data section corresponding to the model, and (d) synthetic seismograms corresponding to the model.

the Bundesanstalt für Geowissenschaften und Rohstoffe (BGR) seismic data presented here [Franke *et al.*, 2008] (Figure 4). The deeper geometry is obtained from the distribution of Wadati-Benioff zone hypocenters. The global relocated hypocenter catalog (January 1964 to December 1995) was used together with 3 additional years of data available online [Engdahl *et al.*, 1998]. Additionally, data from relocated aftershocks were taken to help constrain the plate interface in the 30–50 km depth range [Engdahl *et al.*, 2007]. Together, these data are used to construct the 2-D finite element grid.

[32] We used finite element (FE) software developed by K. Wang [Wang *et al.*, 1995]. The 500 km long FE model consists of 936 quadrilateral elements, with a total of 2933 nodes. The models include the effects of radiogenic heating in the crust, shear heating along the subduction interface (to a distance of 240 km from the trench) for an effective shear stress of 10 MPa, and viscous corner flow in the mantle wedge. Thermal conductivity in the mantle and oceanic crust is 3.138 W/mK consistent with the GDH1 model [Stein and Stein, 1992] and thermal conductivity in the

continental crust is 2.5 W/mK [Peacock and Wang, 1999]. Heat generation in the upper continental crust is 2.5 mW/m² and in the lower continental crust is 0.27 mW/m². Models with lower radioactive heat generation (1.3 mW/m²) resulted in nearly the same thermal structure at depth (along the plate interface), but predict a significantly lower surface heat flow than that observed in the arc and back-arc region. Thus, the higher value was selected in agreement with recent work [Hippchen and Hyndman, 2008]. The model geometry is shown in Figure 18.

[33] The initial boundary conditions include: at the left side, oceanic lithosphere isotherms for a subducting oceanic plate of the appropriate age based on the GDH1 thermal cooling model [Stein and Stein, 1992], 0°C at the surface and an appropriate continental geotherm at the right-side boundary (representing the upper plate). The three primary input parameters to the model are thus; the plate geometry, the age of the subducting lithosphere and the subduction velocity.

[34] The modeled transect is located on the NW Sumatra margin, in the epicentral region of the 26 December 2004

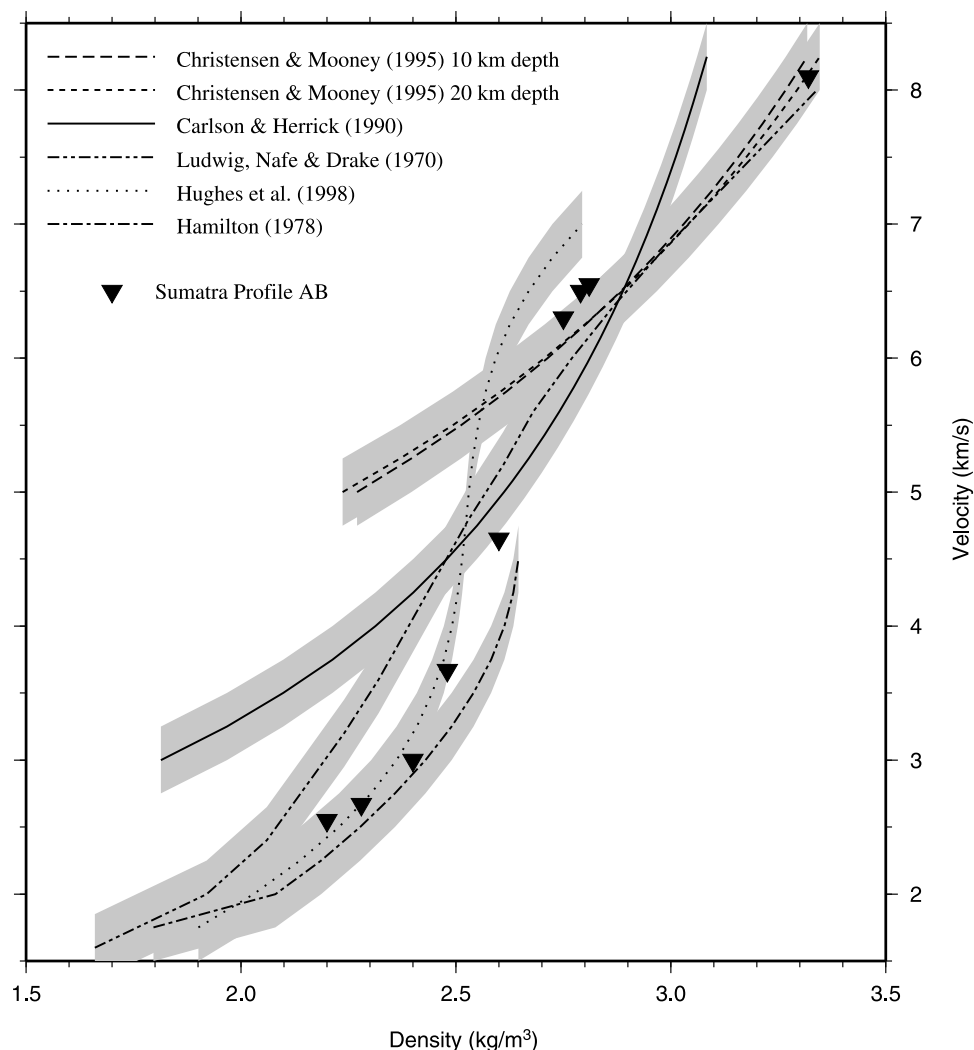


Figure 16. Relationship between velocity and density from various publications. Inverted triangles mark velocity and corresponding densities used for gravity modeling. Shaded areas mark the error bounds of 0.25 km/s.

earthquake. The age of the subducting oceanic lithosphere is known from magnetic anomaly studies [Mueller *et al.*, 1997] and is approximately 60 Ma. At the northern tip of Sumatra, the relative plate motion between the Australian plate and the Sunda block is 5 cm/yr in a N8°E azimuth and the motion between the Indian plate and the Sunda block is 4 cm/yr in a N20°E direction [Vigny *et al.*, 2005]. The component of plate motion perpendicular to the margin thus yields an orthogonal subduction velocity of 3 cm/yr, which was used as the preferred velocity for the thermal modeling.

4.1. Comparison of Observed and Calculated Heat Flow

[35] Heat flow data are available in the study area from several different sources. Older marine and terrestrial heat flow values were obtained from the Global Heat Flow Database (<http://www.heatflow.und.edu>). Marine heat flow data were acquired during the *Marion Dufresne* Aftershocks cruise [Sibuet, 2005] and are shown here. Two other heat flow studies performed during the R/V *Sonne* cruise 189, one with in situ measurements, and one obtained from BSR

observations (calculated using gas-hydrate stability conditions) are also included here [Delisle and Zeibig, 2007]. The observed heat flow pattern (Figure 19a) shows a fairly high degree of scatter, but some general trends are discernable. In the undisturbed oceanic domain, heat flow is about 60 mW/m². Three lower heat flow values near the trench (30–40 mW/m²) are likely due to the cooling effect of hydrothermal fluid circulation as observed in other subduction zone environments [Grevemeyer *et al.*, 2005]. Here the effect appears to be local and not representative of large-scale lithospheric cooling as described for the Central American trench [Harris and Wang, 2002], since the mean heat flow in this region (from the oceanic crust to the toe of the wedge) is about 60 mW/m², the value expected for typical 60 Ma oceanic lithosphere. Heat flow in the fore arc generally declines to values in the 40–60 mW/m², though there is wide scatter in the observed data, with some measurements as high as 80 mW/m². An increase in heat flow is observed in the arc and back arc region to values of 80–90 mW/m², as reported for other back arcs [Currie and Hyndman, 2006].

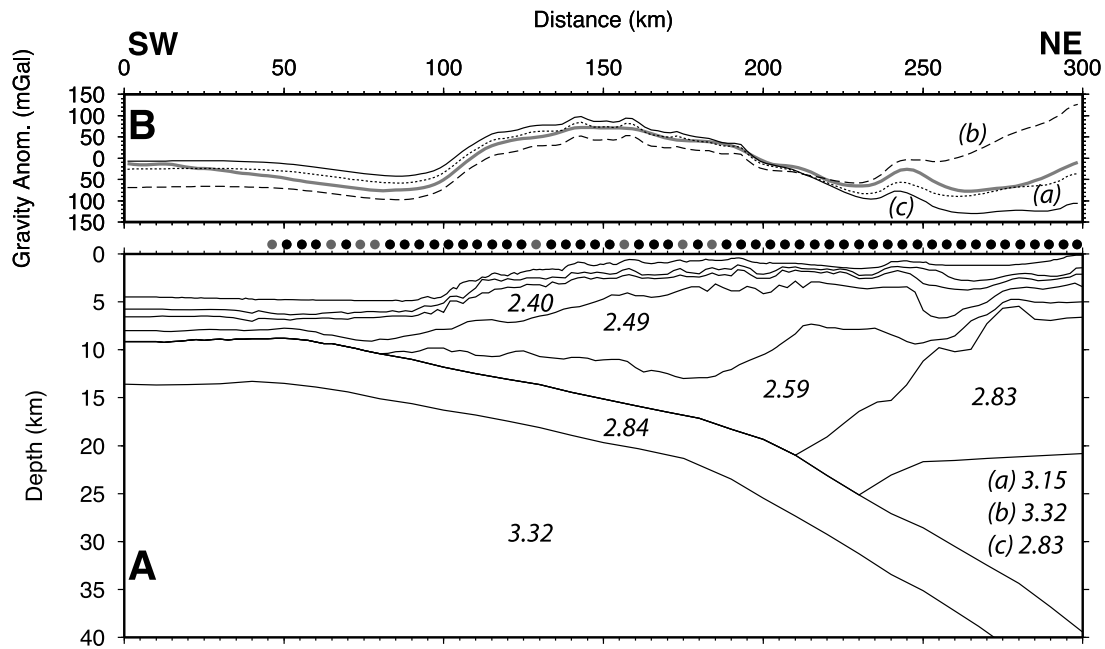


Figure 17. Results from gravity modeling. (a) Gravity model with densities used for modeling in g/cm^3 indicated by italic numbers. Positions of OBSs (dots) are indicated. Solid lines represent layer boundaries from seismic modeling. (b) Shipboard-measured free-air gravity anomaly (gray line). Predicted anomaly for our preferred model is marked by a dotted line, a model in which the mantle wedge has been replaced by continental crust (2.83 kg/m^3) is marked by a black line, and a model where the mantle wedge has been replaced by normal mantle material (3.32 kg/m^3) is marked by a dashed line.

[36] The expected heat flow at the surface calculated using the thermal model presented here is shown in Figure 19a. The calculated 60 mW/m^2 at the trench is in fairly good agreement with the observed data. A decline to about 40 mW/m^2 is predicted in the fore arc, followed by an increase to 80 mW/m^2 in the arc region. No data are available

to check the modeled heat flow predicted for the on-land portion of the fore arc.

4.2. Thermal Structure and the Seismogenic Zone

[37] The modeled thermal structure is presented in Figure 19b. The OBS velocity model as well as the hypocenters

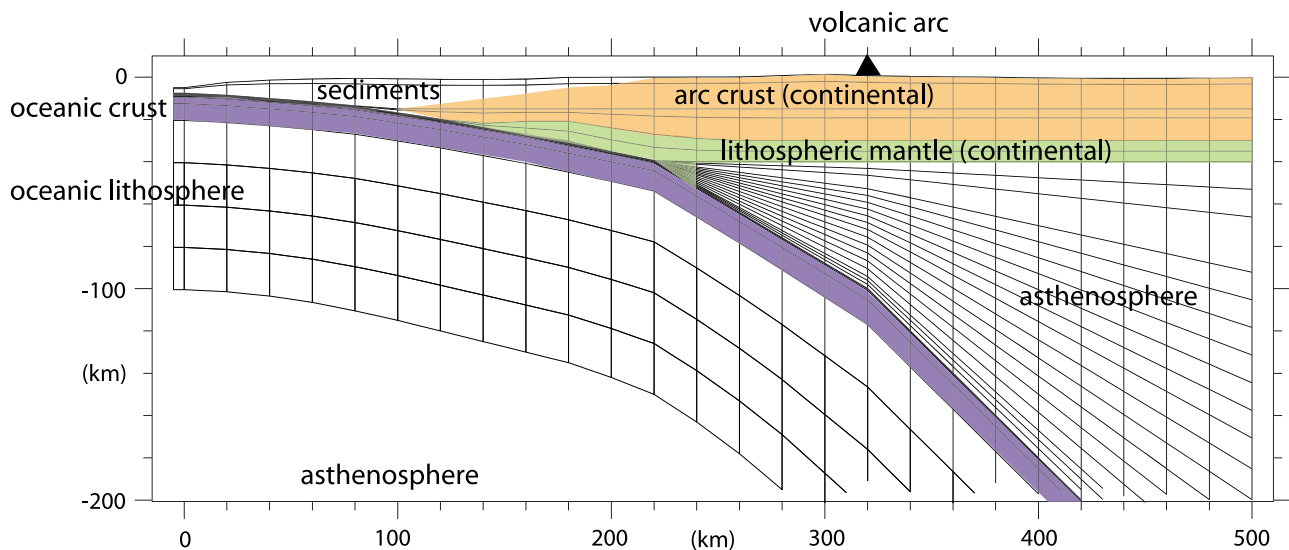


Figure 18. Finite element grid used for calculating fore-arc thermal structure. The three most important factors controlling the thermal structure are the age of the subducting oceanic lithosphere, the convergence velocity, and the geometry of the subduction zone. The model includes radiometric heating in the crust, shear heating along the plate boundary, and convection in the asthenospheric wedge beneath the arc (using a Bachelor’s corner flow solution).

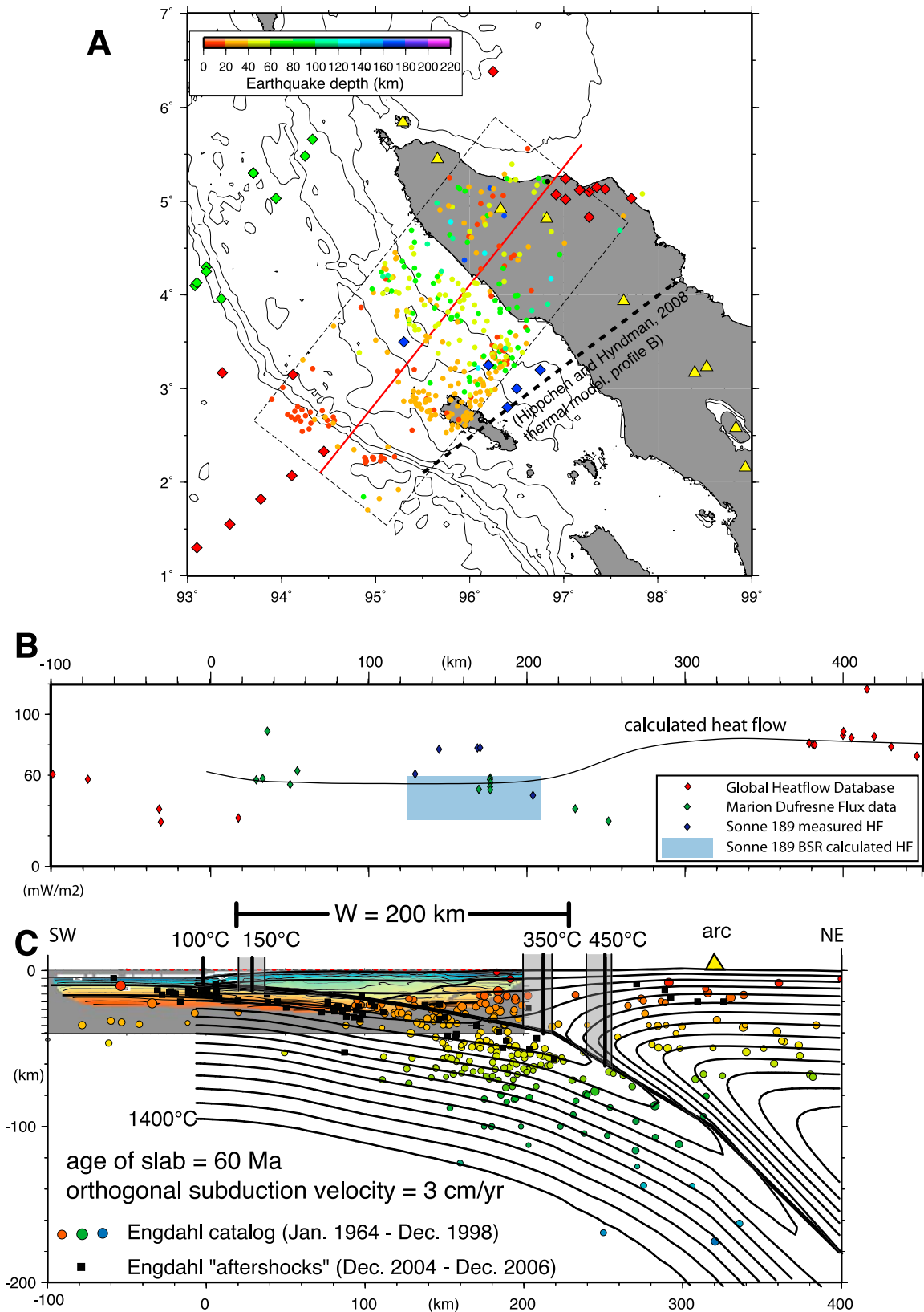


Figure 19

used to constrain the modeled geometry, are shown as well. On the basis of the 100–150°C isotherms, the updip limit is predicted to be very close to the trench (within 5–30 km). This appears to be due to the insulating effect of the thick sedimentary cover at the trench. The thermally predicted position of the updip limit is in good agreement with the observation of numerous aftershocks with a shallow thrusting mechanism in this zone (Figure 14c) [Engdahl *et al.*, 2007]. These results are also in agreement with a recently published thermal model of the NW Sumatra margin located roughly 100–200 km farther SE [Hippchen and Hyndman, 2008] which also predicts an updip limit near the trench. Their 150°C isotherm is 34 km from the trench. For the range of models we tested, we obtained a 150°C isotherm 30 ± 10 km from the trench. Our 350°C and 450°C isotherms, which are considered to correspond to the down-dip limit, are located 210 km and 250 km from the trench axis, respectively. The thermal model further SW (at the limit between the 2004 and 2005 earthquakes) predicts the location of the 350°C and 450°C isotherms at distances of 214 km and 254 km, respectively [Hippchen and Hyndman, 2008], which is nearly identical to the results we obtain. Aftershocks are observed near the shallow dipping plate boundary up to a distance of 220 km from the trench [Engdahl *et al.*, 2007], which is once again in good agreement with the thermally predicted limits.

5. Discussion

[38] Tomographic inversion and forward modeling of wide-angle seismic data from a line located close to the epicenter zone of the great earthquake of December 2004 allows imaging of the accretionary prism and subducted slab to a depth of 35 km (Figures 9 and 10). The accretionary prism shows sedimentary layers with a total thickness of 20 km. Four kilometers of sediments overlie the oceanic crust at the trench, probably consisting of hemipelagic sediments and trench fill. The seismic velocities of the deeper layers are up to 5.5 km/s high, probably owing to compaction and to some low- to middle-grade metamorphic reactions. Sedimentary velocities of the forward model are taken from isovelocity contours of the tomographic model. They roughly correspond to lines of equal lithostatic pressure. As one single sedimentary layer recognized in the MCS data might be characterized by lower velocities where its position is shallow and higher velocities in regions where

its position is deeper, the velocity contours do not coincide exactly with the deep sedimentary layer stratification imaged by the reflection seismic data. In the Simeulue fore-arc basin the isovelocity contours show a pronounced depression, following in general the Neogene basin fill geometry as described by Berglar *et al.* [2008].

[39] The oceanic crust imaged by the reflection or wide-angle seismic data is only about 5 km thick (Franke *et al.* [2008], Singh *et al.* [2008], and this paper) and substantially thinner than “normal” oceanic crust, which is characterized by a thickness of 7.1 ± 0.8 km [White *et al.*, 1992]. Velocities range from 5.80 to 6.80 km/s at the trench to 6.20–6.60 km/s at 270 km model distance. The oceanic Moho found from wide-angle seismic modeling is located at the lower boundary of a series of prominent, discontinuous reflectors in the reflection seismic data. Unusually thin oceanic crust is known to form at ultra slow spreading centers, where serpentinized mantle material commonly outcrops at the seafloor [Jackson *et al.*, 1982; Muller *et al.*, 1997; Jokat and Schmidt-Aursch, 2007]. The oceanic crust currently subducting beneath the NW Sumatra margin was formed around 50–60 Ma at the Wharton spreading center at a half spreading rate between 50 and 75 mm/yr [Royer and Sandwell, 1989]. Thus, very slow spreading can be ruled out to have formed the thin oceanic crust. Alternatively the thickness of the crust might be explained by an unusually low mantle potential temperature at the spreading center leading to low degrees of partial melting in the mantle [Klein and Langmuir, 1987].

[40] The velocities in the oceanic upper mantle are reduced at model distances between 0 and 140 km, with values of 7.40 to 7.60 km/s (Figure 10). A similar reduction in upper mantle velocities was observed offshore Costa Rica over the flexurally faulted portion of the oceanic Cocos plate before it enters the Middle America trench and interpreted as being due to serpentinization of the uppermost mantle [Grevemeyer *et al.*, 2007] through faults generated by the flexure and imaged on seismic reflection data [Ranero *et al.*, 2003]. The oceanic crust at this location offshore Central America formed at the fast spreading East Pacific Rise and is unusually thin (4.8–5.5 km thick) [Grevemeyer *et al.*, 2007]. These thicknesses are very close to those obtained by modeling of the OBS profile off NW Sumatra presented here (Figure 10) and are also observed by the MCS data (Figure 4). It is likely that thin oceanic crust may be fractured more readily and therefore may

Figure 19. Thermal model of the Sumatra subduction zone. (a) Location of the thermal modeling profile (red line), earthquake hypocenters used to construct the model geometry (colored dots), heat flux measurements (colored diamonds), and active volcanoes (triangles). (b) Heat flux (HF) measurement (diamonds), calculated heat flux from depth of a bottom simulating reflector (BSR) (light blue zone), and calculated heat flow (black line) shown along transect from thermal model shown in Figure 19c. (c) Thermal structure along the transect (shown in Figure 1). The geometry is constrained by the reflection and wide-angle seismic data in the shallow portion (0–20 km depth) and by earthquake hypocenters (dots) in the deeper portion. The thermally predicted seismogenic zone has a downdip width of roughly 200 km (180 km taking only the 150°C and 350°C isotherms; 240 km when including the transition zones to 100°C and 450°C). The gray shaded regions indicate the variation in the horizontal (downdip) position of the 150°C, 350°C, and 450°C isotherms for the range of models tested ($v = 2, 3, \text{ and } 4$ cm/yr, and slab ages of 50, 60, and 80 Ma) and is thus a measure of uncertainty. Note that the 100°C isotherm shifts less than 2 km for all models tested. The updip limit extends very close to the trench, beneath most of the accretionary wedge. The downdip portion extends well into the fore-arc mantle of the upper plate. The thermally predicted limits are in good agreement with the observed distribution of relocated aftershocks (black squares) [Engdahl *et al.*, 2007].

permit a higher degree of serpentization in the upper mantle than thick oceanic crust.

[41] We find a strong reflection from a crustal unit at a distance starting 120 km (220 km model distance) from the trench and extending landward (Figure 15). This backstop is characterized by a rough surface showing several blocks and velocities between 6.30 km/s at its top and 6.80 km/s at its base. These velocities and the relatively low velocity gradient of this layer can be characteristic of either igneous continental crust [Christensen and Mooney, 1995] or highly metamorphosed sediments. The corresponding continental Moho is located at a shallow depth of 22 km, similar to that proposed by Kieckhefer *et al.* [1980] from wide-angle seismic modeling of trench parallel profiles near Nias island and by Simoes *et al.* [2004] from gravity modeling of a profile south of Nias island. Both of these studies are located in the segment ruptured during the March 2005 earthquake.

[42] An earlier study based solely on multichannel seismic data acquired by Western Geco, draws the conclusion that the 26 December 2004 earthquake ruptured along a shallow dipping fault beneath the oceanic Moho [Singh *et al.*, 2008]. Both the Western Geco seismic line and the seismic data presented in Figure 4 show clear evidence of folding and thrusting of recently deposited trench fill sediments at the toe of the accretionary wedge. Several of these thrust faults, showing both landward and seaward vergence, can be traced down to a decollement level within the sediments, roughly 1 km above the oceanic basement. These observations suggest that the vast majority of strain from relative plate motion is accommodated here, along the decollement beneath the accretionary wedge and above the downgoing oceanic crust, as observed in all subduction zones worldwide. Megathrust earthquake rupture along this decollement and deep into the sub-fore-arc mantle offers the most coherent explanation for the 26 December 2004 event.

[43] The thermal model presented here predicts a seismogenic zone extending down to 40 km depth and a distance of 220 km from the trench. On the basis of the OBS velocity model, this is well below the fore-arc crust (which has a thickness of about 20 km at a distance of 170 km from the trench). This structural peculiarity is ascertained by several pieces of evidence and supporting elements: (1) the mantle velocity anomaly below the fore arc is shown to be robust through several tomographic inversion runs starting from fairly different initial models, (2) the mantle velocity anomaly below the fore arc is also shown to be necessary to model reflections from the oceanic plate subducting below (Figures 14 and 15), (3) the observation of reflected phases corresponding to this shallow Moho can be modeled as well [Dessa *et al.*, 2009], and (4) a similarly shallow mantle anomaly on favorably oriented profiles is reported in the Nias basin, some 350 km south of our study zone [Kieckhefer *et al.*, 1980].

[44] Together with the seismic data on deep structure, the thermal modeling permits us to assess the hypothesis that either temperatures of 350–450°C or the sub-fore-arc Moho defines the downdip limit of the seismogenic zone, whichever is shallower [Hyndman *et al.*, 1997]. The seismic velocity model clearly indicates that the Moho is shallower than the observed downdip extent of the seismogenic zone (as defined by aftershocks). This does not support the

hypothesis that the Moho is its downdip limit. Our results imply that a significant portion (>50 km) of the rupture occurred along the interface between the oceanic crust of the downgoing plate and the fore-arc mantle of the upper plate. This contradicts the conclusions of a recent thermal modeling study, which suggested that the 30 km deep downdip limit was controlled by the presence of a serpentized mantle wedge beneath the continental Moho [Hippchen and Hyndman, 2008]. Indeed, until now, the 1994 Sanriku-Oki earthquake was the best documented example of a subduction earthquake which ruptured into the sub-fore-arc upper mantle [Hino *et al.*, 2000]. Here, in the Northeast Japan subduction zone, a *M*7.7 event occurred and the detailed aftershock distribution was obtained by deploying a network of OBS on the seafloor. The aftershocks extended to 50 km depth and the upper plate Moho is known from deep crustal seismic studies to be located at 20 km depth [Hino *et al.*, 2000]. A recent review of the seismogenic zone around the Japanese Islands confirms this tendency (deep, sub-Moho rupture) for the northern Honshu and Kanto portions of the Japan trench [Seno, 2005]. The recent Tokachi-oki *M*8 earthquake of 2003 offshore Hokaido also exhibited very deep rupture (40–55 km) [Machida *et al.*, 2009].

[45] Our thermal model also predicts a very shallow updip limit of the seismogenic zone extending almost all the way to the trench and thus implies a very large downdip width of the seismogenic zone (about 200 km). While the exact extent of the updip portion of the rupture plane is difficult to determine precisely [Wang and He, 2008], the results obtained using several different methods all agree that the southernmost portion of the 2004 rupture zone, off NW Sumatra was the widest, about 200 km. These methods include source time studies of fault slip along the plate boundary fault [Ammon *et al.*, 2005], fault slip inversions using geodetic data [Vigny *et al.*, 2005] and tsunami inversions [Fujii and Satake, 2007]. The great downdip width of 200 km is in agreement with that predicted by our thermal modeling and can partly explain the great contribution to seismic moment, owing to the large surface area of the fault plane.

6. Conclusions

[46] Combined modeling of wide-angle and seismic and reflection seismic data of a profile located close to the epicentral area of the great Sumatra earthquake reveals the crustal structure of the subduction zone down to a depth of 35 km. The main structures imaged by this data set are as follows: (1) a total of 4–5 km of sediments overlaying the oceanic crust at the trench, probably consisting of older sediments and trench infill; (2) an anomalously thin oceanic crust, about 5 km thick (although most thin oceanic crust forms at very slow spreading centers, the oceanic crust in this region formed around 50–60 Ma ago at the Wharton spreading center at a fast spreading rate); (3) a backstop structure located about 120 km from the trench beneath the fore-arc basin and characterized by seismic velocities and gradients characteristic of continental crust; (4) a shallow continental Moho at only around 22 km depth, 170 km from the trench; and (5) the hypocenter of the great 2004 earthquake, located at the interface between the downgoing plate and the upper plate continental mantle, indicating that

the mantle wedge is not serpentinized to a degree sufficient to prevent earthquake nucleation.

[47] Thermal modeling of the subduction zone was performed using the crustal structure from the wide-angle seismic data and the distribution of aftershocks. These results indicate the following:

[48] 1. The upper limit of the seismogenic zone (as defined by the 100–150°C isotherms) is located close to the trench (within 5–30 km). This is in good agreement with the observation of numerous aftershocks with a shallow thrusting mechanism in this zone.

[49] 2. The 350°C and 450°C isotherms are located 210 and 250 km from the trench axis, respectively. This corresponds to the landward limit of aftershocks along the fault plane. This limit is about 50 km farther landward and 18 km deeper than the sub-fore-arc Moho.

[50] 3. A significant portion (>50 km) of the rupture occurred along the interface between the oceanic crust of the downgoing plate and the fore-arc mantle of the upper plate. Thus, the downdip limit of seismogenic rupture off NW Sumatra is not controlled by the sub-fore-arc Moho but appears to be controlled by temperatures of 350–450°C isotherms, at which felsic rocks begin to deform by ductile flow.

[51] **Acknowledgments.** Oceanographic work in Indonesia was made possible thanks to the strong involvement of the Indonesian Institute of Sciences (LIPI) and the Agency for the Assessment and Application of Technology (BPPT). French Agence Nationale de Recherche (ANR), Institut National des Sciences de l'Univers (INSU), and Institut français de recherche pour l'exploitation de la mer (Ifremer) contributed to the funding of the SUMATRA-OBS cruise. We would like to thank the Institut Paul-Emile Victor (IPEV) for supporting this work. We thank the chief operator H. Leau, the captain F. Duchènes, and the crew of the R/V *Marion Dufresne* for their professional work during the oceanographic expedition. We would also like to thank the technical teams of the four OBS pools (INSU, Ifremer, University of Brest, and OBIC) and the Genavir technical team for their professional work during the deployment of ocean bottom instruments and the air gun array. We also thank the master and crew operating R/V *Sonne* during MCS data acquisition. The German Ministry for Research and Education (BMBF) supported the study (grant 03G0186A). The GMT [Wessel and Smith, 1995] and Seismic Unix software package [Stockwell, 1999] were used in the preparation of this paper. We thank Bob Engdahl for providing his relocated teleseismic events in the Sumatra region. We thank Roy Hyndman, an anonymous reviewer, and the Associate Editor Kelin Wang for their exhaustive and highly detailed reviews and for the opportunity to improve the manuscript accordingly.

References

- Ammon, C. J., et al. (2005), Rupture process of the 2004 Sumatra-Andaman earthquake, *Science*, *308*, 1133–1139, doi:10.1126/science.1112260.
- Araki, E., M. Shinohara, K. Obana, T. Yamada, Y. Kaneda, T. Kanazawa, and K. Suyehiro (2006), Aftershocks distribution of the 26 December 2004 Sumatra-Andaman earthquake from ocean bottom seismographic observation, *Earth Planets Space*, *58*(2), 113–119.
- Avedik, F., V. Renard, J. P. Allenou, and B. Morvan (1993), "Single bubble" air-gun array for deep exploration, *Geophysics*, *58*, 366–382, doi:10.1190/1.1443420.
- Berglar, K., C. Gaedicke, R. Lutz, D. Franke, and Y. S. Djajadihardja (2008), Neogene subsidence and stratigraphy of the Simeulue forearc basin, Northwest Sumatra, *Mar. Geol.*, *253*, 1–13, doi:10.1016/j.margeo.2008.04.006.
- Byrne, D. E., D. M. Davis, and L. R. Sykes (1988), Loci and maximum size of thrust earthquakes and the mechanics of the shallow region of subduction zones, *Tectonics*, *7*, 833–857, doi:10.1029/TC007i004p00833.
- Byrne, T., and D. Fisher (1990), Evidence for a weak and overpressured decollement beneath sediment-dominated accretionary prisms, *J. Geophys. Res.*, *95*, 9081–9097, doi:10.1029/JB095iB06p09081.
- Carlson, R. L., and C. N. Herrick (1990), Densities and porosities in the oceanic crust and their variations with depth and age, *J. Geophys. Res.*, *95*, 9153–9170, doi:10.1029/JB095iB06p09153.
- Chauhan, A. P. S., S. C. Singh, N. D. Hananto, H. Carton, F. Klingelhoefer, J.-X. Dessa, H. Permana, N. J. White, and D. Graindorge (2009), Seismic imaging of forearc backthrusts at northern Sumatra subduction zone, *Geophys. J. Int.*, *179*(3), 1772–1780, doi:10.1111/j.1365-246X.2009.04378.x.
- Christensen, N. I., and W. D. Mooney (1995), Seismic velocity structure and composition of the continental crust: A global view, *J. Geophys. Res.*, *100*, 9761–9788, doi:10.1029/95JB00259.
- Cohen, J. K., and J. W. Stockwell (2003), *Seismic Unix Release 37: A Free Package for Seismic Research and Processing*, Cent. for Wave Phenomena, Colo. Sch. of Mines, Golden, Colo.
- Curray, J. R., G. G. Shor, R. W. Raitt, and M. Henry (1977), Seismic refraction and reflection studies of the crustal structure of the Eastern Sunda and Western Banda Arcs, *J. Geophys. Res.*, *82*, 2479–2489, doi:10.1029/JB082i017p02479.
- Currie, C. A., and R. D. Hyndman (2006), The thermal structure of subduction zone back arcs, *J. Geophys. Res.*, *111*, B08404, doi:10.1029/2005JB004024.
- Currie, C. A., R. D. Hyndman, K. Wang, and V. Kostoglodov (2002), Thermal models of the Mexico subduction zone: Implications for the megathrust seismogenic zone, *J. Geophys. Res.*, *107*(B12), 2370, doi:10.1029/2001JB000886.
- Davis, D., J. Suppe, and F. Dahlen (1983), Mechanics of fold and thrust belts and accretionary wedges, *J. Geophys. Res.*, *88*, 1153–1172, doi:10.1029/JB088iB02p01153.
- Delisle, G., and M. Zeibig (2007), Marine heat flow measurements in hard ground offshore Sumatra, *Eos Trans. AGU*, *88*(4), doi:10.1029/2007EO040004.
- Dessa, J. X., S. Operto, S. Kodaira, A. Nakanishi, G. Pascal, K. Uhira, and Y. Kaneda (2004), Deep seismic imaging of the eastern Nankai trough, Japan, from multifold Ocean Bottom Seismometer data by combined traveltimes tomography and prestack depth migration, *J. Geophys. Res.*, *109*, B02111, doi:10.1029/2003JB002689.
- Dessa, J.-X., F. Klingelhoefer, D. Graindorge, C. André, H. Permana, M.-A. Gutscher, A. Chauhan, and S. Singh (2009), Megathrust earthquakes can nucleate in the forearc mantle: Evidence from the 2004 Sumatra event, *Geology*, *37*, 659–662, doi:10.1130/G25653A.1.
- Engdahl, E. R., R. D. van der Hilst, and R. Buland (1998), Global teleseismic earthquake relocation with improved travel times and procedures for depth relocation, *Bull. Seismol. Soc. Am.*, *88*, 722–743.
- Engdahl, E. R., A. Villasenor, H. R. DeShon, and C. H. Thurber (2007), Teleseismic relocation and assessment of seismicity (1918–2005) in the region of the 2004 Mw 9.0 Sumatra-Andaman and 2005 Mw 8.6 Nias Island great earthquakes, *Bull. Seismol. Soc. Am.*, *97*, 43–61, doi:10.1785/0120050614.
- Franke, D., M. Schnabel, S. Ladage, D. R. Tappin, S. Neben, Y. S. Djajadihardja, C. Mueller, H. Kopp, and C. Gaedicke (2008), The great Sumatra-Andaman earthquakes: Imaging the boundary between the ruptures of the great 2004 and 2005 earthquakes, *Earth Planet. Sci. Lett.*, *269*, 118–130, doi:10.1016/j.epsl.2008.01.047.
- Fujii, Y., and K. Satake (2007), Tsunami source of the 2004 Sumatra-Andaman earthquake and the Indian Ocean tsunami, *Bull. Seismol. Soc. Am.*, *97*, 192–207, doi:10.1785/0120050613.
- Gailler, A., P. Charvis, and E. Flueh (2007), Segmentation of the Nazca and South American plates along the Ecuador subduction zone from wide angle seismic profiles, *Earth Planet. Sci. Lett.*, *260*, 444–464, doi:10.1016/j.epsl.2007.05.045.
- Graindorge, D., G. Spence, P. Charvis, J. Y. Collot, R. Hyndman, and A. M. Tréhu (2003), Crustal structure beneath the Strait of Juan de Fuca and southern Vancouver Island from seismic and gravity analyses, *J. Geophys. Res.*, *108*(B10), 2484, doi:10.1029/2002JB001823.
- Graindorge, D., et al. (2008), Impact of the lower plate on upper plate deformation at the NW Sumatran convergent margin from seafloor morphology, *Earth Planet. Sci. Lett.*, *275*, 201–210, doi:10.1016/j.epsl.2008.04.053.
- Grevemeyer, I., N. Kaul, J. L. Diaz-Naveas, H. W. Villinger, C. R. Ranero, and C. Reichert (2005), Heat flow and bending-related faulting at subduction trenches: Case studies offshore of Nicaragua and Central Chile, *Earth Planet. Sci. Lett.*, *236*, 238–248, doi:10.1016/j.epsl.2005.04.048.
- Grevemeyer, I., C. R. Ranero, E. R. Flueh, D. Kläschen, and J. Bialas (2007), Passive and active seismological study of bending-related faulting and mantle serpentinization at the Middle America Trench, *Earth Planet. Sci. Lett.*, *258*, 528–542, doi:10.1016/j.epsl.2007.04.013.
- Gutscher, M.-A., and S. M. Peacock (2003), Thermal models of flat subduction and the rupture zone of great subduction earthquakes, *J. Geophys. Res.*, *108*(B1), 2009, doi:10.1029/2001JB000787.
- Hamilton, E. L. (1978), Sound velocity-density relations in the sea-floor sediments and rocks, *J. Acoust. Soc. Am.*, *63*, 366–377, doi:10.1121/1.381747.

- Harris, R. N., and K. Wang (2002), Thermal models of the Middle America Trench at the Nicoya Peninsula, Costa Rica, *Geophys. Res. Lett.*, *29*(21), 2010, doi:10.1029/2002GL015406.
- Henstock, T., L. McNeill, and D. R. Tappin (2006), Seafloor morphology of the Sumatran subduction zone: Surface rupture during megathrust earthquakes?, *Geology*, *34*(6), 485–488, doi:10.1130/22426.1.
- Hino, R., S. Ito, H. Shiobara, H. Shimamura, T. Sato, T. Kanazawa, J. Kasahara, and A. Hasegawa (2000), Aftershock distribution of the 1994 Sanriku-oki earthquake (Mw 7.7) revealed by ocean bottom seismographic observation, *J. Geophys. Res.*, *105*, 21,697–21,710, doi:10.1029/2000JB900174.
- Hippchen, S., and R. D. Hyndman (2008), Thermal and structural models of the Sumatra subduction zone: Implications for the megathrust seismogenic zone, *J. Geophys. Res.*, *113*, B12103, doi:10.1029/2008JB005698.
- Hubbert, M. K., and W. W. Rubey (1959), Role of fluid pressure in mechanics of overthrust faulting, *Geol. Soc. Am. Bull.*, *70*, 115–206, doi:10.1130/0016-7606(1959)70[115:ROFPI]2.0.CO;2.
- Hughes, S., P. J. Barton, and D. Harrison (1998), Exploration in the Shetland-Faeroe Basin using densely spaced arrays of ocean-bottom seismometer, *Geophysics*, *63*(2), 328–334, doi:10.1190/1.1444350.
- Hyndman, R. D. (2007), The seismogenic zone of subduction thrust faults: What we know and don't know, in *The Seismogenic Zone of Subduction Thrust Faults, MARGINS Theor. Exp. Earth Sci. Ser.*, edited by T. H. Dixon and J. C. Moore, pp. 15–40, Columbia Univ. Press, New York.
- Hyndman, R. D., and K. Wang (1993), Thermal constraints on the zone of major thrust earthquake failure: The Cascadia Subduction Zone, *J. Geophys. Res.*, *98*, 2039–2060, doi:10.1029/92JB02279.
- Hyndman, R. D., and K. Wang (1995), The rupture zone of Cascadia great earthquakes from current deformation and the thermal regime, *J. Geophys. Res.*, *100*, 22,133–22,154, doi:10.1029/95JB01970.
- Hyndman, R. D., M. Yamano, and K. Wang (1995), Thermal constraints on the seismogenic portion of the southwestern Japan subduction thrust, *J. Geophys. Res.*, *100*, 15,373–15,392, doi:10.1029/95JB00153.
- Hyndman, R. D., M. Yamano, and D. A. Oleskevich (1997), The seismogenic zone of subduction thrust faults, *Isl. Arc*, *6*, 244–260, doi:10.1111/j.1440-1738.1997.tb00175.x.
- Izart, A., B. Mustafa Kemal, and J. A. Malod (1994), Seismic stratigraphy and subsidence evolution of the northwest Sumatra fore-arc basin, *Mar. Geol.*, *122*, 109–124, doi:10.1016/0025-3227(94)90207-0.
- Jackson, H. R., I. Reid, and R. K. H. Falconer (1982), Crustal structure near the Arctic mid-ocean ridge, *J. Geophys. Res.*, *87*, 1773–1783, doi:10.1029/JB087iB03p01773.
- Johnson, J. M., K. Satake, S. R. Holdahl, and J. Sauber (1996), The 1964 Prince William Sound earthquake: Joint inversion of tsunami and geodetic data, *J. Geophys. Res.*, *101*, 14,965–14,991.
- Jokat, W., and M. Schmidt-Aursch (2007), Geophysical characteristics of the ultra-slow spreading Gakkel Ridge, Arctic Ocean, *Geophys. J. Int.*, *168*(3), 983–998, doi:10.1111/j.1365-246X.2006.03278.x.
- Karig, D. E., M. B. Lawrence, G. F. Moore, and J. R. Curran (1980), Structural framework of the fore-arc basin, NW Sumatra, *J. Geol. Soc.*, *137*, 77–91, doi:10.1144/gsjgs.137.1.0077.
- Khazaradze, G., A. Qamar, and H. Dragert (1999), Tectonic deformation in western Washington from continuous GPS measurements, *Geophys. Res. Lett.*, *26*, 3153–3156, doi:10.1029/1999GL010458.
- Kieckhefer, R. M., G. G. Shor, and J. R. Curran (1980), Seismic refraction studies of the Sunda Trench and Forearc Basin, *J. Geophys. Res.*, *85*, 863–889, doi:10.1029/JB085iB02p00863.
- Klein, E. M., and C. H. Langmuir (1987), Global correlations of ocean ridge basalt chemistry with axial depth and crustal thickness, *J. Geophys. Res.*, *92*, 8089–8115, doi:10.1029/JB092iB08p08089.
- Kopp, H., E. R. Flueh, D. Klaeschen, J. Bialas, and C. Reichert (2001), Crustal structure of the central Sunda margin at the onset of oblique subduction, *Geophys. J. Int.*, *147*(2), 449–474, doi:10.1046/j.0956-540x.2001.01547.x.
- Kopp, H., D. Klaeschen, E. R. Flueh, and J. Bialas (2002), Crustal structure of the Java margin from seismic wide-angle and multichannel reflection data, *J. Geophys. Res.*, *107*(B2), 2034, doi:10.1029/2000JB000095.
- Ladage, S., W. Weinrebe, C. Gaedicke, U. Barckhausen, E. R. Flueh, I. Heyde, A. Krabbenhoef, H. Kopp, S. Fajar, and Y. Djajadihardja (2006), Bathymetric survey images structure off Sumatra, *Eos Trans. AGU*, *87*(17), 165, 168.
- Lay, T., et al. (2005), The Great Sumatra-Andaman earthquake of 26 December 2004, *Science*, *308*, 1127–1133, doi:10.1126/science.112250.
- Ludwig, J. W., J. E. Nafe, and C. L. Drake (1970), Seismic refraction, in *The Sea*, vol. 4, pp. 55–84, John Wiley, New York.
- Machida, Y., et al. (2009), Heterogeneous structure around the rupture area of the 2003 Tokachi-oki earthquake (Mw=8.0), Japan, as revealed by aftershock observations using Ocean Bottom Seismometers, *Tectonophysics*, *465*, 164–176, doi:10.1016/j.tecto.2008.11.009.
- Malod, J.-A., and B. M. Kemal (1996), The Sumatra Margin: Oblique subduction and lateral displacement of the accretionary prism, *Geol. Soc. Spec. Publ.*, *106*, 19–28, doi:10.1144/GSL.SP.1996.106.01.03.
- Marone, C., and D. M. Saffer (2007), Fault friction and the upper transition from seismic to aseismic faulting, in *The Seismogenic Zone of Subduction Thrust Faults, MARGINS Theor. Exp. Earth Sci. Ser.*, edited by T. H. Dixon and J. C. Moore, pp. 346–369, Columbia Univ. Press, New York.
- Moore, J. C., and D. Saffer (2001), Updip limit of the seismogenic zone beneath the accretionary prism of southwest Japan: An effect of diagenetic to low-grade metamorphic processes and increasing effective stress, *Geology*, *29*(2), 183–186, doi:10.1130/0091-7613(2001)029<0183:ULOTSZ>2.0.CO;2.
- Moore, J. C., et al. (1995), Abnormal fluid pressures and fault-zone dilation in the Barbados accretionary prism: Evidence from logging while drilling, *Geology*, *23*(7), 605–608, doi:10.1130/0091-7613(1995)023<0605:AFPAFZ>2.3.CO;2.
- Mueller, D., W. R. Roest, J.-Y. Royer, L. M. Gahagan, and J. G. Sclater (1997), Digital isochrons of the world's ocean floor, *J. Geophys. Res.*, *102*, 3211–3214, doi:10.1029/96JB01781.
- Muller, M. R., C. J. Robinson, T. A. Minshull, R. S. White, and M. J. Bickle (1997), Thin crust beneath ocean drilling program borehole 735B at the southwest Indian Ridge?, *Earth Planet. Sci. Lett.*, *117*, 295–317.
- Oleskevich, D. A., R. D. Hyndman, and K. Wang (1999), The updip and downdip limits to great subduction earthquakes: Thermal and structural models of Cascadia, south Alaska, SW Japan, and Chile, *J. Geophys. Res.*, *104*, 14,965–14,991, doi:10.1029/1999JB000060.
- Pacheco, J. F., L. R. Sykes, and C. H. Scholz (1993), Nature of seismic coupling along simple plate boundaries of the subduction type, *J. Geophys. Res.*, *98*, 14,133–14,159, doi:10.1029/93JB00349.
- Peacock, S. M., and K. Wang (1999), Seismic consequences of warm versus cool subduction zone metamorphism: Examples from northeast and southwest Japan, *Science*, *286*, 937–939, doi:10.1126/science.286.5441.937.
- Ramachandran, K., R. D. Hyndman, and T. M. Brocher (2006), Regional P wave velocity structure of the Northern Cascadia Subduction zone, *J. Geophys. Res.*, *111*, B12301, doi:10.1029/2005JB004108.
- Ranero, C. R., J. Phipps Morgan, K. McIntosh, and C. Reichert (2003), Bending-related faulting and mantle serpentinization at the Middle America Trench, *Nature*, *425*, 367–373, doi:10.1038/nature01961.
- Royer, J.-Y., and D. T. Sandwell (1989), Evolution of the eastern Indian Ocean since the Late Cretaceous: Constraints from Geosat altimetry, *J. Geophys. Res.*, *94*, 13,755–13,782, doi:10.1029/JB094iB10p13755.
- Ruff, L., and H. Kanamori (1980), Seismicity and the subduction process, *Phys. Earth Planet. Inter.*, *23*, 240–252, doi:10.1016/0031-9201(80)90117-X.
- Saffer, D. M., and B. A. Bekins (2002), Hydrological controls on the morphology and mechanics of accretionary wedges, *Geology*, *30*(3), 183–186.
- Sandwell, D., and W. Smith (1995), Marine gravity from satellite altimetry, version 7.2, ftp: baltica.ucsd.edu, Geol. Data Cent., Scripps Inst. of Oceanogr., La Jolla, Calif.
- Satake, K. (1993), Depth distribution of coseismic slip along the Nankai Trough, Japan, from joint inversion of geodetic and tsunami data, *J. Geophys. Res.*, *98*, 4553–4565, doi:10.1029/92JB01553.
- Satake, K., K. Shimazaki, Y. Tsuji, and K. Ueda (1996), Time and size of a giant earthquake in Cascadia inferred from Japanese tsunami records of January 1700, *Nature*, *379*, 246–249, doi:10.1038/379246a0.
- Savage, J. C. (1983), A dislocation model of strain accumulation and release at subduction zones, *J. Geophys. Res.*, *88*, 4984–4996, doi:10.1029/JB088iB06p04984.
- Schlüter, H. U., C. Gaedicke, H. A. Roeser, B. Schreckenberger, H. Meyer, C. Reichert, Y. Djajadihardja, and A. Prexl (2002), Tectonic features of the southern Sumatra-western Java forearc of Indonesia, *Tectonics*, *21*(5), 1047, doi:10.1029/2001TC901048.
- Scholz, C. H. (1990), *The Mechanics of Earthquakes and Faulting*, 439 pp., Cambridge Univ. Press, Cambridge, U.K.
- Seno, T. (2005), Variation of downdip limit of the seismogenic zone near the Japanese islands: Implications for the serpentinization mechanism of the forearc mantle wedge, *Earth Planet. Sci. Lett.*, *231*, 249–262, doi:10.1016/j.epsl.2004.12.027.
- Sibuet, J.-C. (2005), MD/149 Sumatra aftershocks on board *Marion Dufresne*, *OCE/2005/04*, Inst. Paul-Emile Victor, Plouzané, France.
- Sibuet, J.-C. (2007), 26th December 2004 great Sumatra-Andaman earthquake: Co-seismic and post-seismic motions in northern Sumatra, *Earth Planet. Sci. Lett.*, *263*, 88–103, doi:10.1016/j.epsl.2007.09.005.
- Simoes, M., J. P. Avouac, R. Cattin, and P. Henry (2004), The Sumatra subduction zone: A case for a locked fault zone extending into the mantle, *J. Geophys. Res.*, *109*, B10402, doi:10.1029/2003JB002958.
- Singh, S. C., et al. (2008), Seismic evidence for broken oceanic crust in the 2004 Sumatra earthquake epicentral region, *Nature Geosci.*, *1*(11), 777–781, doi:10.1038/ngeo336.

- Stanley, D., and A. Villasenor (2000), Models of downdip frictional coupling for the Cascadia megathrust, *Geophys. Res. Lett.*, *27*, 1551–1554, doi:10.1029/1999GL005441.
- Stein, C. A., and S. Stein (1992), A model for the global variation in oceanic depth and heat flow with lithospheric age, *Nature*, *359*, 123–126, doi:10.1038/359123a0.
- Stein, S., and E. A. Okal (2005), Speed and size of the Sumatra earthquake, *Nature*, *434*, 581–582, doi:10.1038/434581a.
- Stockwell, J. W. (1999), The CWP/SU: Seismic Unix package, *Comput. Geosci.*, *25*(4), 415–419, doi:10.1016/S0098-3004(98)00145-9.
- Tichelaar, B. W., and L. J. Ruff (1993), Depth of seismic coupling along subduction zones, *J. Geophys. Res.*, *98*, 2017–2037, doi:10.1029/92JB02045.
- Vigny, C., et al. (2005), Insight into the 2004 Sumatra-Andaman earthquake from GPS measurements in southeast Asia, *Nature*, *436*, 201–206, doi:10.1038/nature03937.
- Vrolijk, P. (1990), On the mechanical role of smectite in subduction zones, *Geology*, *18*(8), 703–707, doi:10.1130/0091-7613(1990)018<0703:OTMROS>2.3.CO;2.
- Wang, K., and J. He (2008), Effects of frictional behavior and geometry of subduction fault on coseismic seafloor deformation, *Bull. Seismol. Soc. Am.*, *98*, 571–579, doi:10.1785/0120070097.
- Wang, K. L., R. D. Hyndman, and M. Yamano (1995), Thermal regime of the southwest Japan subduction zone: Effects of the age history of the subducting plate, *Tectonophysics*, *248*, 53–69, doi:10.1016/0040-1951(95)00028-L.
- Wells, D. L., and K. J. Coppersmith (1994), New empirical relationships among magnitude, rupture length, rupture width, rupture area, and surface displacement, *Bull. Seismol. Soc. Am.*, *84*, 974–1002.
- Wessel, P., and W. H. F. Smith (1995), New version of the generic mapping tools released, *Eos Trans. AGU*, *76*(33), 329, doi:10.1029/95EO00198.
- White, R. S., D. McKenzie, and R. O’Nions (1992), Oceanic crustal thickness from seismic measurements and rare earth element inversions, *J. Geophys. Res.*, *97*, 19,683–19,715, doi:10.1029/92JB01749.
- Zelt, C. A. (1999), Modelling strategies and model assessment for wide-angle seismic traveltimes data, *Geophys. J. Int.*, *139*(1), 183–204, doi:10.1046/j.1365-246X.1999.00934.x.
- Zelt, C. A., and P. J. Barton (1998), Three-dimensional seismic refraction tomography: A comparison of two methods applied to data from the Faroe Basin, *J. Geophys. Res.*, *103*, 7187–7210, doi:10.1029/97JB03536.
- Zelt, C. A., and R. B. Smith (1992), Seismic travel time inversion for 2-D crustal velocity structure, *Geophys. J. Int.*, *108*(1), 16–31, doi:10.1111/j.1365-246X.1992.tb00836.x.

C. André, D. Graindorge, and M.-A. Gutscher, UMR 6538, Domaines Océaniques, Université de Bretagne Occidentale, Institut Universitaire Européen de la Mer, Place Nicolas Copernic, F-29280 Plouzané, France. (david.graindorge@univ-brest.fr)

A. Chauhan, Laboratoire de Géosciences Marines, Institut de Physique du Globe de Paris, 4, place Jussieu, Case 89, F-75252 Paris, France. (chauhan@ipgp.jussieu.fr)

J.-X. Dessa, Géosciences Azur, UMR 6526, Observatoire Océanologique de Villefranche, Université Pierre et Marie Curie, CNRS, Port de la Darse, BP 48, F-06235, Villefranche sur Mer, France. (dessa@geoazur.obs-vlfr.fr)

D. Franke and S. Ladage, Federal Institute for Geosciences and Natural Resources, Stilleweg 2, D-30655 Hanover, Germany. (dieter.franke@bgr.de; stefan.ladage@bgr.de)

F. Klingelhoefer, Department of Marine Geosciences, Ifremer, BP 70, Plouzané F-29280, France. (fklingel@ifremer.fr)

H. Permana, Earth Dynamics and Geological Disaster Division, Research Center for Geotechnology, Indonesia Institute of Sciences, Bandung 40132, Indonesia. (permh@yaho.com)

T. Yudistira, Program Studi Teknik Geofisika, Institut Teknologi Bandung, Gd. Basic Science B Lt. 4, Jl. Ganesa 10, Bandung 40132, Indonesia. (tdyudistira@yahoo.com)